DTU Library

Human in-vivo brain magnetic resonance current density imaging (MRCDI)

Göksu, Cihan; Hanson, Lars G. ; Siebner, Hartwig R; Ehses, Philipp; Scheffler, Klaus; Thielscher, Axel

Published in:
NeuroImage

Link to article, DOI:
10.1016/j.neuroimage.2017.12.075

Publication date:
2017

Document Version
Peer reviewed version

Accepted Manuscript

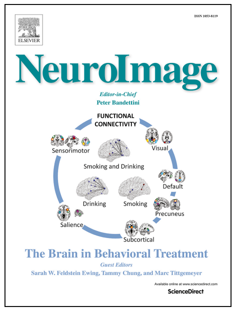

Human in-vivo brain magnetic resonance current density imaging (MRCDI)

Cihan Göksu, Lars G. Hanson, Hartwig R. Siebner, Philipp Ehses, Klaus Scheffler, Axel Thielscher

PII: S1053-8119(17)31099-6

DOI: 10.1016/j.neuroimage.2017.12.075

Reference: YNIMG 14590

To appear in: *NeuroImage*

Received Date: 1 November 2017

Accepted Date: 22 December 2017

Please cite this article as: Göksu, C., Hanson, L.G., Siebner, H.R., Ehses, P., Scheffler, K., Thielscher, A., Human in-vivo brain magnetic resonance current density imaging (MRCDI), *NeuroImage* (2018), doi: 10.1016/j.neuroimage.2017.12.075.

Human In-vivo Brain Magnetic Resonance Current Density Imaging (MRCDI)

Cihan Göksu[1,2], Lars G. Hanson[1,2], Hartwig R. Siebner[1,5], Philipp Ehses[3,6], Klaus Scheffler[3,4†], and Axel Thielscher[1,2,3†*]

[1] Danish Research Centre for Magnetic Resonance, Centre for Functional and Diagnostic Imaging and Research, Copenhagen University Hospital Hvidovre, Denmark.

[2] Center for Magnetic Resonance, DTU Elektro, Technical University of Denmark, Kgs Lyngby, Denmark.

[3] High-Field Magnetic Resonance Center, Max-Planck-Institute for Biological Cybernetics, Tübingen, Germany.

[4] Department of Biomedical Magnetic Resonance, University of Tübingen, Tübingen, Germany.

[5] Department of Neurology, Copenhagen University Hospital, Bispebjerg, Denmark.

[6] German Center for Neurodegenerative Diseases (DZNE), Bonn, Germany

[†] These authors contributed equally to this work.

***** Corresponding Author
Axel Thielscher, Assoc. Prof.
Danish Research Centre for Magnetic Resonance, Centre for Functional and Diagnostic Imaging and Research, Copenhagen University Hospital Hvidovre, Section 714, Kettegaard Allé 30, 2650 Hvidovre, Denmark.
Tel: + 45-38623326
e-mail: axelt@drcmr.dk

ABSTRACT

Magnetic resonance current density imaging (MRCDI) and MR electrical impedance tomography (MREIT) are two emerging modalities, which combine weak time-varying currents injected via surface electrodes with magnetic resonance imaging (MRI) to acquire information about the current flow and ohmic conductivity distribution at high spatial resolution. The injected current flow creates a magnetic field in the head, and the component of the induced magnetic field $\Delta B_{z,c}$ parallel to the main scanner field causes small shifts in the precession frequency of the magnetization. The measured MRI signal is modulated by these shifts, allowing to determine $\Delta B_{z,c}$ for the reconstruction of the current flow and ohmic conductivity.

Here, we demonstrate reliable $\Delta B_{z,c}$ measurements in-vivo in the human brain based on multi-echo spin echo (MESE) and steady-state free precession free induction decay (SSFP-FID) sequences. In a series of experiments, we optimize their robustness for in-vivo measurements while maintaining a good sensitivity to the current-induced fields. We validate both methods by assessing the linearity of the measured $\Delta B_{z,c}$ with respect to the current strength. For the more efficient SSFP-FID measurements, we demonstrate a strong influence of magnetic stray fields on the $\Delta B_{z,c}$ images, caused by non-ideal paths of the electrode cables, and validate a correction method. Finally, we perform measurements with two different current injection profiles in five subjects. We demonstrate reliable recordings of $\Delta B_{z,c}$ fields as weak as 1 nT, caused by currents of 1 mA strength. Comparison of the $\Delta B_{z,c}$ measurements with simulated $\Delta B_{z,c}$ images based on FEM calculations and individualized head models reveals significant linear correlations in all subjects, but only for the stray field-corrected data. As final step, we reconstruct current density distributions from the measured and simulated $\Delta B_{z,c}$ data. Reconstructions from non-corrected $\Delta B_{z,c}$ measurements systematically overestimate the current densities. Comparing the current densities reconstructed from corrected $\Delta B_{z,c}$ measurements and from simulated $\Delta B_{z,c}$ images reveals an average coefficient of determination R^2 of 71%. In addition, it shows that the simulations underestimated the current strength on average by 24%.

Our results open up the possibility of using MRI to systematically validate and optimize numerical field simulations that play an important role in several neuroscience applications, such as transcranial brain stimulation, and electro- and magnetoencephalography.

Key words:

Current-induced magnetic field, magnetic resonance current density imaging, multi-echo spin echo, steady-state free precession free induction decay, in-vivo imaging

INTRODUCTION

Accurate knowledge of the current flow distribution in the human head caused by neural or external sources is important in several neuroscience applications such as targeting control in transcranial brain stimulation (TBS) and source localization in electro- (EEG) and magnetoencephalography (MEG) (Mosher et al., 1999; Nitsche and Paulus, 2000). The current distributions are usually derived using forward modeling schemes that employ volume conductor models of the head (Oostenveld et al., 2011; Tadel et al., 2011; Thielscher et al., 2015). However, even anatomically accurate models of the head still suffer from uncertainties of the tissue conductivities. The conductivity values reported in literature vary substantially across studies, likely caused by both methodological differences and natural physiological variability, with the amount of uncertainty depending on the tissue type (Dabek et al., 2016; Faes et al., 1999; Huang et al., 2017; Miranda, 2013). Methods to measure the current flow non-invasively in-vivo are thus important for the validation and improvement of these forward modelling approaches.

Magnetic resonance current density imaging (MRCDI) and MR electrical impedance tomography (MREIT) are two emerging modalities, which combine weak time-varying currents injected via surface electrodes with magnetic resonance imaging (MRI) to acquire information about the current flow and ohmic conductivity at high spatial resolution (Eyüboğlu, 2006a, 2006b; Göksu et al., 2014; Joy, 2004; Scott et al., 1991; Seo and Woo, 2011; Woo et al., 1994). In short, the injected current flow creates a magnetic field in the head, and the component of the induced magnetic field $\Delta B_{z,c}$ parallel to the main magnetic field of the scanner slightly changes the precession frequency of the magnetization (here, the z-axis is chosen along the static scanner field, and $\Delta B_{z,c}$ is correspondingly the current-induced field change). This modulates the phase of the measured MRI signal proportional to $\Delta B_{z,c}$. The current-induced phase changes can thus be used to determine $\Delta B_{z,c}$, and to reconstruct the inner current flow and the ohmic conductivity distribution (Eyüboğlu, 2006b, 2006c; Ider and Birgül, 1998; Joy, 2004; Oh et al., 2003; Scott et al., 1991; Seo and Woo, 2011).

Up to now, successful MRCDI and MREIT recordings have been demonstrated in phantoms, animal models and in-vivo in human limbs (Birgül et al., 2003; Eyüboğlu, 2006c; Han et al., 2010; Ider and Birgül, 1998; Jeon et al., 2009; Jeong et al., 2010; Kim et al., 2009, 2008, 2011; Meng et al., 2012; Oh et al., 2005, 2003; Sadighi et al., 2014; Sadleir et al., 2005; Seo and Woo, 2011; Woo and Seo, 2008). However, in order to achieve a sufficient signal-to-noise ratio (SNR) of the $\Delta B_{z,c}$ images, these studies applied current strengths that were much higher than those applicable for in-vivo human brain applications (1-2 mA; Utz et al., 2010). Only recently, the first proof-of-principle studies have been performed that demonstrated the feasibility of acquiring $\Delta B_{z,c}$ images for the human brain in-vivo using weak current strengths (Jog et al., 2016; Kasinadhuni et al., 2017). These initial results are promising, but highlight the need for further improvements of the measurement procedures and sequences to allow for sufficient quality and unambiguous $\Delta B_{z,c}$ images in a reasonable acquisition time.

Using comprehensive theoretical analyses and phantom measurements, we have previously optimized the sensitivity of two MRI sequences for in-vivo MRCDI and MREIT measurements in the human brain (Göksu et al., 2017). We explored multi-echo spin echo (MESE) and steady-state free precession free induction decay (SSFP-FID) sequences, and derived optimized parameters to maximize their efficiency for measuring current-induced phase changes, given relaxation parameters of brain tissue at 3 T. Here, we validate the performance of the optimized sequences for in-vivo brain imaging and improve their robustness to artifacts that are of concern in an in-vivo setting, in order to ensure the validity of the results. Using the adapted approach, we perform measurements with two different current injection profiles in five subjects using SSFP-FID, and demonstrate reliable recordings of $\Delta B_{z,c}$ fields as weak as 1 nT. We compare the $\Delta B_{z,c}$ measurements with simulations based on the Finite-Element Method (FEM) and individualized head models reconstructed from structural MR images of the same subjects. As final step, we reconstruct the current flow distributions from both the measured and simulated $\Delta B_{z,c}$ data. Taken together, the results presented here highlight the importance of careful validation of the measurement procedures to ensure unambiguous current density reconstructions. They optimize the novel $\Delta B_{z,c}$ measurements for in-vivo applications, and pave the way for their application in future MRCDI and MREIT studies of the human brain.

METHODS

Subjects

Thirteen healthy subjects were included in the study, which consisted of five successive experiments. Five participants took part in two of the experiments, and two participated three times. They had no previous history of neurological or psychiatric disorders and were screened for contraindications to MRI and TBS. Written informed consent was obtained from all participants prior to the scans. The study complied with the Helsinki declaration on human experimentation and was approved by the Ethics Committee of the Capital Region of Denmark (H16032361).

Sequence of Experiments

Our study is organized in five successive experiments:

- First, we compare the SNR and quality of $\Delta B_{z,c}$ images acquired with single- vs. multi-gradient-echo readouts. Our prior results demonstrated the need to use long echo times for MESE and long repetition times for SSFP-FID in order to maximize efficiency. The resulting SNR-optimal low readout bandwidth (BW) decreases image quality as it causes considerable distortions particularly for in-vivo applications. Here, we test to which extent these effects can be prevented by using multi-gradient-echo readouts that are acquired at a higher BW and that are subsequently combined to reconstruct the $\Delta B_{z,c}$ image.

- Second, we validate the methods by assessing the linearity of the measured $\Delta B_{z,c}$ with respect to the strength of the injected currents.
- Third, we focus on the more efficient SSFP-FID measurements and assess the influence of magnetic stray fields on the $\Delta B_{z,c}$ images, caused by non-ideal paths of the feeding cables that are connected to the electrodes. We propose and validate a method to correct for these undesired influences.
- Fourth, we re-evaluate the impact of the chosen repetition times on measurement efficiency and image quality in the presence of physiological noise. We test whether decreasing the repetition times below the theoretically optimal values can help to improve image quality without substantially sacrificing the SNR of the $\Delta B_{z,c}$ images.
- Fifth, we perform $\Delta B_{z,c}$ measurements with two different current injection profiles (right-left and anterior-posterior), and compare the measurements with simulations based on the Finite-Element Method (FEM) and individualized head models reconstructed from structural MR images of the same subjects. We also reconstruct and compare the current density distributions from the measured and simulated $\Delta B_{z,c}$ data. For both the $\Delta B_{z,c}$ images and current flow distributions, we test how much the correction of the cable-induced magnetic stray fields affects the similarity between measured and simulated data.

MRI sequences for MRCDI

We tested the in-vivo application of two different MRCDI sequences, MESE (Fig. 1a) and SSFP-FID (Fig. 1b). Details of the sequences can be found in (Göksu et al., 2017). In short, we selected MESE because of its high SNR for the magnitude images and its robustness to field inhomogeneity (Nam and Kwon, 2010), and SSFP-FID for its high phase sensitivity (Lee et al., 2016; Scheffler et al., 2006).

For MESE (Fig. 1a), the measured current-induced magnetic field for the nth spin-echo $\Delta B_{z,c}^{n}$ is given as

$$\Delta B_{z,c}^{n} = (\angle M_n^{+} - \angle M_n^{-}) / 2\gamma T_{ES} n, \quad (1)$$

where γ is the gyromagnetic ratio of protons, and T_{ES} the echo spacing. The measurement is performed twice with opposite current injection profiles, and $\angle M_n^{+}$ and $\angle M_n^{-}$ are the phases of the acquired complex MR images for the positive and negative current directions for the nth echo (Göksu et al., 2017; Nam and Kwon, 2010; Scott et al., 1992). The final $\Delta B_{z,c}$ image is determined as the weighted sum of the $\Delta B_{z,c}^{n}$ images of the single echoes, with the weightings being proportional to the inverse of the variances of the images (Göksu et al., 2017). When a multi-gradient-echo readout is used, the final $\Delta B_{z,c}$ image is determined in the same way after summation across all acquired gradient echoes.

For SSFP-FID (Fig. 1b), the $\Delta B_{z,c}$ image in case of weak injection currents is given as

$$\Delta B_{z,c} = \frac{\angle M_{SS1} - \angle M_{SS2}}{m_{seq}}, \tag{2}$$

with $\angle M_{SS1}$ and $\angle M_{SS2}$ being the phase images for echoes with positive and negative current injection. The constant $m_{seq} = \partial\left(\angle M_{SS1} - \angle M_{SS2}\right)/\partial \Delta B_{z,c}$ is the phase sensitivity to magnetic field changes (Göksu et al., 2017). We calculated it via spin simulations based on 3D rotation and relaxation matrices (Jaynes, 1955), and it depends on the sequence and tissue relaxation parameters.

Measurement procedures

All experiments were performed on a 3 T MRI scanner (MAGNETOM Prisma, SIEMENS Healthcare, Erlangen, Germany) equipped with a 64-channel head coil. Multi-channel signals were combined using an adaptive combine algorithm that employs a spatial matched filter created from the individual coil images without a-priori knowledge of coil sensitivity maps (Walsh et al., 2000). The electrical current waveforms were created using a waveform generator (33500B; Keysight Technologies, Santa Clara, CA, USA), amplified using an MR-conditional device for transcranial weak current stimulation (DC-STIMULATOR PLUS, neuroConn GmbH, Ilmenau, Germany), and were applied to the participants via circular rubber electrodes (5 cm in diameter) attached to the scalp. We used two different electrode configurations that created current flows either from right to left (R-L) or from anterior to posterior (A-P) in the brain. For R-L current injection, the rubber electrodes were attached symmetrically at positions directly above and slightly anterior to the ears using conductive paste (Ten20, Weaver and Company, Colorado, USA). This corresponds roughly to positions above the temporoparietal junctions. For A-P injection, one electrode was placed centrally on the forehead and the second centrally superior to the inion. Unless stated otherwise, peak current amplitudes of ± 1 mA were used. A ramp up period of 10 s was used in order to prevent sudden subject motion. MR data acquired during this period were discarded.

We used single-slice MESE and SSFP-FID measurements, with an axial slice placed in the upper half of the brain. Based on an initial structural image (details are given below), the slice position was chosen to contain approximately the electrode centers. The fat signal was suppressed by a chemical-shift-selective (CHESS) fat suppression technique (Haase et al., 1985). A field of view (FOV) of 224x180 mm^2, an image matrix of 112x90 and a voxel size of 2x2x3 mm^3 were used for both sequence types. For MESE, the echo spacing was T_{ES} = 60 ms, repetition time was T_R = 1.5 s and the number of spin echoes was N_{SE} = 3. For SSFP-FID, the tip angle was α = 30˚. The other MR sequence parameters varied across experiments and are stated below. All experiments were performed with both positive and negative current directions (i.e. two subsequent acquisitions of each k-space line; the first corresponds to the positive direction and the second to the negative). The current waveforms were employed as indicated in Figure 1 (I_c^+ for the first acquisition and I_c^- for the second). By that, each k-space line was acquired twice in successive readout periods with opposite currents I_c^+ and I_c^- to measure two phase images with opposite current-induced phases. After acquisition of the complete k-space, the measurements were repeated. The MESE measurements were repeated twice (N_{meas} = 2), with a total scan time of $T_{tot} \approx 9$ mins. For SSFP-FID, the number of measurements N_{meas} varied across experiments and are stated below. Generally, they were selected as high as possible while limiting the total duration of each experiment for the participants to 2 hours. This included up to 1 hour 20 minutes of MR scanning (in experiment 2; details are stated below), of which maximally 45 minutes were combined with current stimulation.

For all subjects, a high-resolution structural image was acquired using the Pointwise Encoding Time reduction with Radial Acquisition (PETRA) sequence (Ida et al., 2015) with number of slices N_{sli} = 320, image matrix 320x320, voxel size 0.9x0.9x0.9 mm^3, tip angle $\alpha = 6^\circ$, T_R = 3.61 ms, T_E = 0.07 ms, inversion time T_I = 0.5 s, BW = 359 Hz/pixel, and turbo factor 400. The images exhibited a T_1-weighted contrast for soft tissue. In addition, it allowed locating the rubber of the electrodes and of the cable insulations due to the short T_E. The visibility of the cable tracks was further improved by covering them with Play-Doh (Hasbro Inc., RI, USA) which provides strong MRI signal due to its high water content.

For participants in which the current flow distribution was estimated using FEM calculations, additional T_1- and T_2-weighted images were acquired for the construction of individualized volume conductor models. The T_1-weighted images were based on a Magnetization-Prepared Rapid Acquisition Gradient-Echo (MPRAGE) sequence with number of slices N_{sli} = 208, image matrix 256x256, voxel size 1x1x1 mm^3, tip angle $\alpha = 9^\circ$, T_R = 2700 ms, T_E = 3.63 ms, and inversion time T_I = 1090 ms with selective water excitation. The T_2-weighted images used a Sampling Perfection with Application-optimized Contrasts using different flip-angle Evolutions (SPACE) sequence with N_{sli} = 208, image matrix 256x256, voxel size 1x1x1 mm^3, T_R = 3200 ms, T_E = 408 ms, and turbo factor 282.

Experiment 1: Single- vs. Multi-gradient-echo acquisition

In three participants, we compared the quality and SNR of the $\Delta B_{z,c}$ images based on multi-gradient-echo readouts at high BW versus their single-gradient-echo counterparts at low BW, employing an R-L electrode montage. The experiments were performed both with and without current injection. The MESE experiments were repeated for N_{GE} = 1 (BW = 19.2 Hz/pixel; echo time point relative to the preceding refocusing pulse: T_{GE}=30 ms) and N_{GE} = 5 (BW = 103.6 Hz/pixel; gradient echo time points relative to the preceding refocusing pulse: T_{GE}=[8.8, 19.6, 30, 40.6, 51.2] ms). The SSFP-FID experiments were performed with T_R = 120 ms and N_{meas} = 12 (T_{tot} ≈ 4.5 mins). They were repeated for N_{GE} = 1 (BW = 12 Hz/pixel; gradient echo time point relative to the preceding RF pulse: T_{GE}=60 ms) and N_{GE} = 7 (BW = 75 Hz/pixel; gradient echo time points: T_{GE} = [8.33, 22.43, 36.53, 50.63, 64.73, 79.00, 93.16] ms).

MESE was tested at its optimal T_{ES} of 60 ms, while SSFP-FID was tested at its optimal T_R of 120 ms, resulting in a different number of readouts for the multi-gradient-echo cases. For both sequences, the number of readouts was chosen to result in a BW that was high enough to prevent visible distortions. The quality of the resulting $\Delta B_{z,c}$ images was evaluated by visual inspection. In addition, the performance of the methods was quantified by creating histograms of the noise floor in the $\Delta B_{z,c}$ images acquired without current injection. For that, masks created from the magnitude images were used to extract the values from the brain. Gaussian distributions were fitted to the histograms, and the differences in the mean $\mu_{\Delta Bzc}$ and standard deviation $\sigma_{\Delta Bzc}$ of the fits were evaluated.

Experiment 2: Linear dependence of the measured $\Delta B_{z,c}$ on current strength

In order to verify the linear dependence of the measured $\Delta B_{z,c}$ on the strength of the injected currents, MESE and SSFP-FID experiments using multi-gradient-echo readouts were performed in four participants. The data of one subject was discarded due to severe motion artefacts. For MESE, N_{GE} = 5 was used. The parameters for SSFP-FID were T_R = 120 ms, N_{meas} = 12 and N_{GE} = 7. For each participant, measurements at four currents strength (I_c = 0, 0.33, 0.66 and 1 mA) were acquired in random order, using an R-L electrode montage. This resulted in 4x12=48 SSFP-FID and 4x2=8 MESE measurements per participant. For each measurement, average $\Delta B_{z,c}$ values were extracted from a region-of-interest (ROI) that was individually positioned to exhibit clear current-induced phase changes for the MESE measurements at 1 mA. Linear regression models of the extracted $\Delta B_{z,c}$ values as a function of I_c were fitted both to the MESE and SSFP-FID results, and the mean shifts β_0 and slopes β_1 and their standard errors are reported.

Experiment 3: Correction of cable-induced stray magnetic fields

Given the higher efficiency of SSFP-FID compared to MESE (Göksu et al., 2017), we focused on SSFP-FID in the rest of the study. The sequence parameters were T_R = 120 ms, N_{meas} = 24 (T_{tot} ≈ 9 mins) and N_{GE} = 7. In the proximity of the head, the cables connecting the electrodes to the current stimulator should be fully parallel to the main magnetic field of the scanner. This ensures that the magnetic fields created by the current flow through the cables do not contribute to the phase of the measured MR images. Any deviation from an ideal parallel cable path can result in strong stray fields which change the measured $\Delta B_{z,c}$ distribution. For example, a straight wire of 10 cm length that carries a current of 1 mA and is placed parallel to an axial imaging plane at a distance of 10 cm changes the z-component of the magnetic field in the plane by up to 0.9 nT. This is approximately the situation encountered if the electrode cables meet just above or below the head, and the resulting field change is similar to that caused by current flow inside the head. However, parallel cable paths are difficult to achieve in practice, as modern multi-channel receive coils fit tightly around the head. Changing to, e.g. birdcage coils would strongly reduce the SNR of the measurements. In addition, in our measurements, the stray fields were severe as we employed a twisted wire pair that branched out only in close proximity to the head. This was caused by the need to employ stimulator equipment that was CE approved as medical device.

Using SSFP-FID measurements in four participants, we demonstrated the impact of the cable-induced stray fields on the $\Delta B_{z,c}$ images. A wire loop was placed around the head, with the upper half following a similar path as the cables in the other measurements. The lower half of the loop was extended inferior, with the wires being as parallel as possible to the main magnetic field for 30 cm before they were twisted and connected to the stimulator. By that, the stray field of the wire loop coarsely mimicked that of the cables in the axial imaging slice in the upper part of the head.

In order to correct for the effects of the stray field, we reconstructed the wire path from the PETRA images, calculated the wire-induced field using the Biot-Savart Law, and subtracted it from the measured $\Delta B_{z,c}$ image. We validated this correction method by comparing the corrected $\Delta B_{z,c}$ images with the results of control measurements without current injection. Histograms of both measurements were obtained, and the mean and standard deviation of Gaussian distributions fitted to the histograms were compared. For both the experiments with and without current flow, N_{meas} = 24 measurements were used. The experiments were repeated twice to test the reproducibility of the results.

Experiment 4: Dependence of measurement efficiency on repetition time

In our prior study (Göksu et al., 2017), we employed phantom experiments and simulations to demonstrate a strong influence of the SSFP-FID repetition time T_R (Fig. 1b) on the efficiency of the MRCDI measurements. We derived an optimal value of T_R = 120 ms, which is higher than usually employed in order to allow for sufficient phase accumulation. However, a long T_R can also increase the influence of physiological noise on the measurements, leading us to re-evaluate the impact of T_R on measurement efficiency in the in-vivo case.

We performed SSFP-FID experiments in six participants, employing an R-L electrode montage. The experiments were repeated with and without current injection. The data of one subject was discarded due to severe motion artefacts. In each participant, three repetition times T_R = [40, 80, 120] ms were tested in a random order. The number of measurement repetitions N_{meas} was adjusted to keep the total acquisition time T_{tot} close to 9 mins. The remaining MR sequence parameters were adjusted to optimize the measurement sensitivity and image quality for the given T_R:

- T_R = 40 ms: T_{GE} = 20 ms, N_{GE} = 1, BW = 276 Hz/pixel, N_{meas} = 72
- T_R = 80 ms: T_{GE} = [7.46, 19.73, 31.86, 43.99, 56.13] ms, N_{GE} = 5, BW = 88 Hz/pixel, N_{meas} = 36
- T_R = 120 ms: T_{GE} = [8.33, 22.43, 36.53, 50.63, 64.73, 79.00, 93.16] ms, N_{GE} = 7, BW = 75 Hz/pixel, N_{meas} = 24

The $\Delta B_{z,c}$ images were corrected for the cable-induced stray fields as described above. Histograms of the $\Delta B_{z,c}$ images without current injection were obtained, and the mean and standard deviation of Gaussian distributions fitted to the histograms were determined.

Experiment 5: $\Delta B_{z,c}$ measurements for two different electrode montages

We compared the $\Delta B_{z,c}$ images obtained for R-L versus A-P electrode montages in six participants. The sequence parameters were T_R = 120 ms, N_{meas} = 24 ($T_{tot} \approx 9$ mins) and N_{GE} = 7. The measurements were repeated with and without current injection. The data of one subject was discarded due to motion artefacts. The $\Delta B_{z,c}$ images were corrected for the cable-induced stray fields. Histograms of the $\Delta B_{z,c}$ images without current injection were obtained, and the mean and standard deviation of Gaussian distributions fitted to the histograms were determined.

FEM simulations of the current flow and the induced magnetic field

We compared the $\Delta B_{z,c}$ images measured in experiment 5 with simulated images, using FEM calculations of the current flow distribution inside the head based on our open-source pipeline SimNIBS 2 (www.simnibs.org; A Thielscher et al., 2015). An anatomically realistic volume conductor model was automatically created from the structural T_1 and T_2-weighted MR images. The model consists of five tissue compartments, namely brain gray matter (GM), white matter (WM), cerebrospinal fluid (CSF), skull and scalp. Isotropic ohmic conductivities were assigned to the tissues (WM: 0.126 S/m, GM: 0.275 S/m, CSF: 1.654 S/m, bone: 0.010 S/m, scalp: 0.465 S/m) (Thielscher et al., 2011). The electrode positions were determined from the PETRA images. The electrode pads were modelled as disks with 50 mm diameter and 5 mm thickness with a conductivity of 1.0 S/m. For the FEM calculations, Dirichlet boundary conditions for the electrostatic potential were applied at the electrode surfaces (Saturnino et al., 2015). The simulations were performed for both R-L and A-P montages, assuming a current strength of I_c = 1 mA. The Biot-Savart Law was applied to the calculated current density distribution $\vec{J}$ in order to determine the $\Delta B_{z,c}$ image.

Reconstruction of current density images

The measured $\Delta B_{z,c}$ images for the two electrode montages R-L and A-P (experiment 5) were used to determine current density distributions. We reconstructed the x- and y-component of the current density in the imaging slice using the approach explained in (Ider et al., 2010; Park et al., 2007). The recovered current density $\vec{J}_{rec}$, termed “projected current density” in (Park et al., 2007), is given as

$$\vec{J}_{rec} = \vec{J}_0 + \frac{1}{\mu_0}\left(\frac{\partial(\Delta B_{z,c} - \Delta B^0_{z,c})}{\partial y}, -\frac{\partial(\Delta B_{z,c} - \Delta B^0_{z,c})}{\partial x}, 0\right) \quad (3)$$

with μ_0 being the permeability of free space. The variables $\vec{J}_0$ and $\Delta B^0_{z,c}$ denote the current density and magnetic field distributions that would occur for a uniform conductivity distribution inside the head. They were determined using FEM calculations. The projected current density images were reconstructed from both the measurements with and without stray field correction, and compared with the simulation results. A median filter (3x3 neighborhood) was applied to the $\Delta B_{z,c}$ measurements to remove spatial high-frequency noise before applying the reconstruction algorithm. For comparability, the same filter was applied to the simulated $\Delta B_{z,c}$, even though it affected the images only marginally. There are more advanced filtering (Lee et al., 2011) and current density reconstruction (Ider et al., 2010; Park et al., 2007) techniques, which might perform slightly better. However, they are beyond the scope of this study.

RESULTS

Subject Experiences

For both the MESE and SSFP-FID methods, the synchronized injected current induced similar side effects in each of the subjects. All subjects reported phosphenes, which were stronger for the A-P compared the R-L electrode configuration. They also experienced subtle tingling near the electrodes, which disappeared after a short while. None of the subjects reported any discomfort due to the current injection.

Experiment 1: Single- vs. Multi-gradient-echo acquisition

For both the MESE and SSFP-FID measurements, the evaluation of the $\Delta B_{z,c}$ images acquired without current injection (Fig. 2a) shows that the multi-gradient-echo readouts consistently reduce the noise floor. In case of multiple echoes, the depicted $\Delta B_{z,c}$ images are the weighted sum of the single echo results, with the weighting factors being proportional to the inverse of the variances of the images (Göksu et al., 2017). The better quality of the multi-gradient-echo results is corroborated by the lower mean values and standard deviations obtained for the $\Delta B_{z,c}$ images of the multi-gradient-echo readouts, as listed in Table 1 (Supplementary Fig. S1 shows the corresponding histograms). In this respect, the mean values indicate $\Delta B_{z,c,}$ offsets, while the standard deviations characterize the “noise power”, i.e. the strength of the spatial fluctuations of the noise. As a side note, the MESE measurements with multi-gradient-echo readouts have the lowest noise standard deviations across all four tested conditions. However, it should be noted that the listed values are not normalized per unit time, and the total scan time of MESE was two times longer than that of the SSFP-FID counterparts.

The use of multi-gradient-echo readouts also helps to improve the quality of the MR magnitude images (Supplementary Fig. S2) and $\Delta B_{z,c}$ images obtained with current injection (Fig. 2b). Specifically, the results for the single-gradient-echo readouts suffer from ghosting-like patterns, which are absent when multi-gradient-echo readouts are used. Visual inspection suggests further that the multi-gradient-echo readouts result in more similar $\Delta B_{z,c}$ images for the MESE and SSFP-FID measurements in each of the three subjects.

Experiment 2: Linear dependence of the measured $\Delta B_{z,c}$ on current strength

Figure 3a shows the MR magnitude and $\Delta B_{z,c}$ images for MESE and SSFP-FID measurements performed at I_c = 1 mA. In each of the subjects, the $\Delta B_{z,c}$ images of the MESE and SSFP-FID measurements show a good similarity. Average $\Delta B_{z,c}$ values were extracted from the indicated ROIs for each of the four tested current strengths and plotted against the current strength in Fig. 3b. In all cases, the fitted regression models are highly significant, demonstrating a good linear dependency (Table 2). The mean shifts β_0 (i.e., the intercepts of the fits) are close to zero in all cases, which proves the absence of systematic biases. For all three subjects, the slopes β_1 are similar between the MESE and SSFP-FID results. For SSFP-FID, the small standard errors indicate a good accuracy of the $\Delta B_{z,c}$ results that were obtained by averaging across twelve measurements.

Experiment 3: Correction of cable-induced magnetic stray fields

The $\Delta B_{z,c}$ fields created by currents flowing in a wire loop around the head and measured using SSFP-FID are shown in Fig. 4b. Corrected images were obtained by subtracting $\Delta B_{z,c}$ fields that were determined via forward calculations based on the reconstructed wire paths and the Biot-Savart Law (Fig. 4c).

Comparing the corrected images with control $\Delta B_{z,c}$ measurements without current injection (Fig. 4d) demonstrates that the remaining noise after the correction is in a similar range to that of the control images. This is confirmed by evaluating the mean values and standard deviations of the $\Delta B_{z,c}$ images, as listed in Table 3. For both experimental runs, the mean values of the corrected and control results are close to zero. The standard deviations are slightly higher for the corrected results, indicating a small residual effect that was not corrected by the subtraction procedure. The underlying reason might be small inaccuracies in determining the wire paths from the PETRA images.

Experiment 4: Dependence of SSFP-FID measurement efficiency on repetition time

The $\Delta B_{z,c}$ images acquired using SSFP-FID at three different repetition times, both with and without current injection, are shown in Figure 5. The images with current injection were corrected for the impact of the cable-induced stray fields as described above. The SNR of the images acquired at T_R =

40 ms is clearly lower than obtained at the two other repetition times. The results obtained at T_R = 80 ms and T_R = 120 ms exhibit similar sensitivities to the current-induced magnetic field changes. An exception is the $\Delta B_{z,c}$ image obtained for subject S_4 without current injection (fourth row of Fig. 5a), which has a poor quality compared to the other results, presumably due to motion outside of the imaged slice. This occurred even though the MR magnitude images show no considerable image artifacts (Supplementary Fig. S3). Comparison of the standard deviations of the $\Delta B_{z,c}$ images obtained without current injection confirms the visual impression (Table 4). On average, the standard deviation is reduced by 61% for T_R = 80 ms and 53% for T_R = 120 ms compared to the measurements at T_R = 40 ms. The measurements using T_R = 80 ms perform slightly better than those with T_R = 120 ms in four out of five subjects.

Experiment 5: $\Delta B_{z,c}$ measurements for two different electrode montages

The $\Delta B_{z,c}$ images obtained by SSFP-FID measurements for the R-L and A-P electrode montages are shown in Figure 6, both without (Fig. 6b) and with correction of the cable-induced stray fields (Fig. 6c). Visual comparison confirms the importance of applying the correction (please note, that the blue-red patterns are actually inversed between uncorrected and corrected images). Focusing on the corrected images (Fig. 6c), the results of the A-P montage exhibit very similar spatial distributions of the current-induced magnetic fields across the five subjects, while the obtained peak intensities clearly vary. The results obtained with the R-L montage differ more between subjects, with the variation in the electrode positions likely contributing to these differences.

The control $\Delta B_{z,c}$ images obtained without current injection (Supplementary Fig. S4) exhibit an average mean shift of $\mu_{\Delta Bz,c}$ = 0.005 nT (averaged across the five subjects) and an average standard deviation of $\sigma_{\Delta Bz,c}$ = 0.111 nT. These values ensure a sufficient sensitivity when measuring magnetic field changes caused by the current flow at the chosen strength of 1 mA.

Comparison of measured and simulated current-induced magnetic fields $\Delta B_{z,c}$

We simulated the current-induced magnetic field for both the R-L and A-P electrode montages (Fig. 7a shows exemplarily the results for subject S_1). In general, the simulated and measured fields exhibit similar spatial distributions and variations, supporting the validity of the measurements. Scatter plots of the measurements (with and without correction of the stray fields) versus simulations show clear linear dependencies for the corrected $\Delta B_{z,c}$ data, which are absent for the uncorrected measurements (Fig. 7b depicts the results for S_1). Correspondingly, fitting linear regression models to the dependencies between corrected $\Delta B_{z,c}$ measurements and simulations reveals significant results for all subjects (Table 5), with the coefficients of determination being on average 0.68 and 0.88 for the R-L and A-P montages. Interestingly, the estimated slopes are slightly lower than unity. That is, the simulations underestimate $\Delta B_{z,c}$ slightly, but quite systematically in 9 out of the 10 measurements. It is worth noting that we do not expect identical results, as the simulations were based on a head model that employed standard conductivity values from literature.

Comparison of the current density measurements and simulations

We reconstructed the x- and y-components of the current density distribution in the imaging slice from the $\Delta B_{z,c}$ measurements (with and without stray field correction) and additionally from the simulated $\Delta B_{z,c}$ data in the five subjects for both R-L and A-P electrode montages. The results of the first subject are exemplarily shown in Figure 8a (Supplementary Fig. S5 lists the results of the other subjects). For the simulations, the reconstructed current densities $\vec{J}_{rec}$ differ markedly from the original current densities $\vec{J}_{FEM}$ that were determined via FEM calculations and served to calculate the $\Delta B_{z,c}$ distributions via the Biot-Savart Law. While coarse features of the current flow pattern such as generally higher current densities close to the electrodes and in the longitudinal fissure (for the A-P montage) are maintained, fine inflow effects in the sulci are mostly lost. Visual comparison of the current density reconstructions from the uncorrected versus corrected $\Delta B_{z,c}$ measurements reveals that the current densities close to the electrodes are overestimated when the $\Delta B_{z,c}$ data is not corrected for the cable-induced stray fields. In addition, increased current densities in the CSF-filled longitudinal fissure are only observable for the corrected case. Comparing the current density distributions reconstructed from the measurements versus the simulations by means of scatter plots (Fig. 8b) and linear regression analyses (Tables 6 and 7) confirms that the difference between measurements and simulations is overestimated without stray field correction. Specifically, the slopes of the regression lines increase by on average 0.16 (uncorrected vs. corrected: 0.65 vs. 0.81, pooled across A-P and R-L). Also for the corrected data, the slopes are still lower than unity, i.e. the simulations systematically underestimate the current densities by on average 24%. The coefficients of determination are only slightly increased for the corrected data, for which they reach on average 0.71.

DISCUSSION AND CONCLUSIONS

We tested two MR sequences, MESE and SSFP-FID, for measurements of weak current-induced magnetic fields in the human brain. The sequences were previously optimized using extensive computer simulations and phantom tests (Göksu et al., 2017) to maximize their sensitivity to the current-induced fields. Here, we assessed their performance in-vivo and demonstrated that both sequence types could be successfully used to reveal the magnetic field distributions for a current strength of 1 mA, in turn allowing us to reconstruct the current flow distribution in the brain.

Optimization and validation of the MR sequences and measurement procedures

Our results demonstrated the need to adapt the employed sequences for in-vivo application by including multi-gradient-echo acquisitions. Specifically, long echo times (MESE) and repetitions times (SSFP-FID) are required to maximize the sensitivity of the measurements to the current-induced magnetic fields (Göksu et al., 2017). This in turn decreases their robustness to physiological noise (e.g., due to respiration, blood flow and small subject movement) when single-echo readouts with low bandwidths are used. Our results show that multi-gradient-echo readouts at higher bandwidths improve the image quality and allow selecting long echo and repetition times to maximize sensitivity, even though the total available readout period is slightly shortened by the time needed for the additional gradient switching in that case.

In contrast to the better efficiency of SSFP-FID compared to MESE observed in the prior phantom tests, both sequence types had similar noise levels in the in-vivo case when matching the total acquisition time. Specifically, comparing the average noise standard deviations listed for MESE (N_{GE}=5) in Table 1 to the results for SSFP-FID with T_R = 120 ms in Table 4 (both acquired with $T_{tot} \approx$ 9 mins) reveals similar values. This indicates that physiological noise is a dominant factor that limits the sensitivity of the in-vivo measurements. In practice, the higher number of measurements that are obtained during SSFP-FID acquisitions open up a possibility of discarding (partial) measurements with strong noise, thereby possibly improving the quality of the final averaged magnetic field image. Nevertheless, MESE may still outperform SSFP-FID in multi-slice acquisition, as it allows for interleaved slice excitation without prolonging the total acquisition time (Göksu et al., 2017). The impact of physiological noise also became apparent when testing different repetition times for the SSFP-FID measurements. As expected, increasing T_R from 40 ms to 80 ms increased the measurement sensitivity. However, an additional increase to 120 ms tended to decrease the sensitivity of the in-vivo results slightly again, in contrast to the theoretical and phantom results. This indicates that a T_R moderately below the theoretically optimal value can be chosen for in-vivo applications without losing sensitivity, while potentially improving robustness.

For both sequence types, the dependence of the measured magnetic field on the current strength exhibited a good linearity. In each of the three tested subjects, the slopes of the linear fits of the results obtained with the two sequences were similar. This validates the chosen scaling factor m_{seq} for the SSFP-FID measurements (Eq. 2), which relates the magnetic field and phase changes, and which was determined via spin simulations (Göksu et al., 2017).

We have demonstrated strong effects of the magnetic stray fields created by the current flow in the cables on the measured magnetic field and on the reconstructed current flow distributions, and have validated a correction method that employs delineations of the cable paths derived from structural images for forward calculations of the stray fields. While improved cable designs might help to ameliorate this problem, we would like to emphasize that even a small deviation from an ideal path parallel to the field direction of the scanner will cause non-negligible distortions of the measured field distributions when it occurs close to the measurement volume, e.g., 10 cm away. This effect results in miscalculated current flow distributions, and highlights the importance of controlling for and, if required, correcting the impact of the stray fields.

Comparison of measured and simulated fields

The measured magnetic fields showed a good correspondence to the fields obtained via FEM simulations, with average coefficient of determinations R^2 of 68% and 88% for R-L and A-P montages. Following up on the reasons why the A-P montage is on average revealing a better correspondence might be interesting for future studies. The simulations based on "standard" tissue conductivities taken from literature systematically underestimated the strength of the current-induced $\Delta B_{z,c}$ in 9 out of the 10 measurements (average regression slopes of 0.80 and 0.90 for R-L and A-P). Also the current density distributions estimated from the corrected magnetic field measurements and the FEM simulations were in good agreement, with an average coefficient of determination of R^2=71%, with little difference between the R-L and A-P montages. The simulations underestimated the current strength on average by 24%. The likely main reason are inaccurate ohmic conductivities assigned to the brain tissues in the FEM simulations. In addition, the use of isotropic conductivity values for white matter might affect the accuracy of the simulations, as its conductivity is known to be anisotropic (e.g., Nicholson, 1965). Future studies could therefore test whether the use of conductivity tensors estimated from diffusion MRI (e.g., Opitz et al., 2011) improves the fit between measurements and simulations. Along similar lines, it could be tested whether more detailed models of the pad electrodes (Saturnino et al., 2015) increase the fit. Interestingly, recent studies using invasive in-vivo recordings to measure the electric field injected by transcranial weak current stimulation indicate that FEM simulations based on standard conductivity values similar to the ones used here over- rather than underestimate the electric field strength (Huang et al., 2017; Opitz et al., 2016). This apparent contradiction might be resolved by considering that we reconstructed the current density rather than the electric field. Huang et al. (2017) derived individually optimized ohmic conductivities to best fit the simulated to the measured electric fields, and found that optimization resulted in higher-than-standard tissue conductivities consistently across subjects. Increasing the conductivity of brain tissue would in turn tend to increase the current strength inside the skull, in line with our results. While this explanation seems plausible, it should be followed up, e.g. by future simulation work.

Prior Studies

To our knowledge, only two prior studies report in-vivo MR measurements of current-induced magnetic fields in the human brain. In (Jog et al., 2016), standard field mapping sequences were employed to measure the constant fields of direct currents. While the use of standard sequences has the advantage that 3D coverage can be readily achieved, this approach is not robust to slow temporal drifts of the MR signal that occur due to both technical and physiological reasons, inherently limiting the achievable sensitivity. The results presented in (Kasinadhuni et al., 2017) were based on a measurement approach that was more similar to the approach tested here. However, their method is comparably less sensitive to current-induced field changes and the results were not corrected for cable-induced stray fields. The spatial patterns of the measured magnetic field distributions reported in that study vary substantially across subjects, despite using the same electrode locations. The peak magnetic field values exceed those, which we obtained for the uncorrected images, and are consistently higher than those indicated by their and our FEM simulations. Even when considering that a higher current strength of 1.5 mA was applied, these observations indicate that cable-induced stray fields likely affected the results of that study. As the employed current flow reconstruction algorithm was based on first order spatial derivatives of the measured current-induced magnetic field (Ider et al., 2010; Park et al., 2007), any non-constant stray field will distort the reconstructed current flow. This opens the possibility that also the substantial differences between the measured and simulated current density reconstructions reported in (Kasinadhuni et al., 2017) might have been amplified by neglecting putative cable-induced stray fields. As a side note, the detrimental effects of cable-induced stray fields on the reconstructed current flow do not occur for methods which rely on the Laplacian of $\Delta B_{z,c}$ (e.g., Ider et al., 2010), as the Laplacian of the cable-induced stray magnetic fields is zero inside the imaging region. However, as these methods employ second derivatives, they might suffer more from amplified noise in the reconstructed current density images.

Limitations and Future Work

The main focus of our study was on the optimization and validation of the MR sequences and measurement protocol. In the future, the measurement sensitivity can possibly be further increased by using pulse sequences such as balanced alternating steady-state free precession (bSSFP) which exhibits a more than 10 times higher phase sensitivity (Bieri et al., 2006; Minhas et al., 2010). A higher sensitivity would be beneficial to limit scan time when aiming to extend the spatial coverage towards multiple slices. Increasing the current strength from 1 mA up to 2 mA is also feasible, but requires careful piloting. Stronger currents also increase the side effects such as tickling and pain sensations underneath the electrodes, which makes the measurements less comfortable for the participants and might result in stronger head movement. In addition, the correction method for the cable-induced stray field used here requires manual tracking of the cable paths that are, however, well visible as dark regions inside the bright Play-Doh. The tracking accuracy depends on the spatial resolution of the employed PETRA images (0.9 mm iso-voxel in our experiments, which is sufficiently small to guarantee sufficient accuracy). It would be desirable to optimize the cable design in order to reduce the influence of the cable-induced stray fields, which might help to further increase the robustness of the final results.

The employed current density reconstruction can be further optimized. The observed similarity between the reconstructions from measured and simulated data suggests that the method in its current form is already sufficient to obtain a coarse approximation of the current flow. Replacing the median filter used to denoise the $\Delta B_{z,c}$ image before applying the reconstruction algorithm by more advanced filter approaches (Lee et al., 2011) might help to reveal some more detail in the reconstructed current density images. The reconstruction was based on the simplifying assumption that the x- and y-components of the current-induced magnetic field are small and can be neglected (Sajib et al., 2012). This also implies that the measured conductivity distribution does not vary along the z-direction. However, the head and brain clearly vary along z, so that accurate estimations of the current flow require assumptions that are more realistic. Combined with the imaging of multiple slices, reconstructing the current flow from 3D $\Delta B_{z,c}$ data should help to increase the accuracy of the reconstruction (Ider et al., 2010). However, it should be noted that these limitations do not affect our finding that the FEM simulations underestimated the current strength, as we applied the same reconstruction steps to the simulation results rather than using the originally simulated current distribution for comparison (Fig. 8a). Finally, it will be interesting to explore the usage of the measured $\Delta B_{z,c}$ data for the estimation of individual tissue conductivities (Kwon et al., 2016).

Conclusion

We have demonstrated the feasibility of reliable MRCDI measurements in-vivo in the human brain at a current strength of 1 mA. Future studies might aim to further improve the sensitivity of the MR methods and their robustness to physiological noise, as well as to extend their spatial coverage towards multiple slices. Our results are promising and indicate that MRCDI measurements combined with the reconstruction of current densities and tissue conductivities (Eyüboğlu, 2006c; Ider et al., 2010; Park et al., 2007; Seo et al., 2003; Seo and Woo, 2011) might be useful for validating simulations based on volume conductor models of the head and for improving the accuracy of the simulations.

ACKNOWLEDGEMENTS

This study was supported by the Lundbeck foundation (grant R118-A11308 to AT and grant R59 A5399 to HR).

FIGURE CAPTIONS

Figure 1. Schematic diagrams of the MESE and SSFP-FID sequences (please see Göksu et al., 2017 for details). (a) Diagram of the MESE sequence. The sequence is composed of a 90˚ excitation pulse preceding repetitive 180˚ refocusing pulses, so that multiple spin echoes are created. The injected bipolar current waveform is synchronized with the radio frequency (RF) pulses, so that the phase of the continuous complex transverse magnetization ($\measuredangle\mu$) increases linearly over time. The measurement is performed twice with opposite current injection profiles (indicated by red and green dashed lines), and the difference between the phase images is used to determine the current-induced magnetic field. Either single-gradient-echo readouts (single G_r) or multi-gradient-echo readouts with fly-back (multi G_r) are used. (b) Diagram of the SSFP-FID sequence. The sequence is composed of repetitive in-phase excitation pulses with constant tip angle and constant repetition time T_R. A bipolar current waveform is injected in synchrony with the SSFP-FID sequence. The current-induced phase of the continuous complex transverse magnetization evolves in opposite directions in odd and even T_R periods (indicated by red and green lines), which results in two different steady-state conditions with opposite phases. Either single-gradient-echo readouts (single G_r) or multi-gradient-echo readouts with fly-back (multi G_r) are used.

Figure 2. Experiment 1: Comparison of single- vs. multi-gradient-echo acquisition in three subjects. The T_{ES} (MESE) and T_R (SSFP-FID) times were kept identical between both cases. All images are shown in radiological convention, with the orientation indicated for the lower right slice in subfigure b. (a) $\Delta B_{z,c}$ images of the measurements without current injection. For both MESE and SSFP-FID (T_R=120 ms, N_{meas} = 12), the results of the multi-gradient-echo acquisitions exhibit a lower noise floor than those of the single-gradient-echo acquisitions. (b) $\Delta B_{z,c}$ images of the measurements with current injection. For better visualization of the spatial patterns, mean-corrected images are shown (i.e., the average $\Delta B_{z,c}$ in the brain was subtracted). The quality of the images is improved by the use of multi-gradient-echo readouts, which prevent the ghosting-like patterns observed in the results of the single-gradient-echo acquisitions. Please note that the total acquisition times differed for MESE ($T_{tot} \approx 9$ mins) and SSFP-FID ($T_{tot} \approx 4.5$ mins) in this experiment, as the primary goal was to compare single-versus multi-gradient-echo readouts.

Figure 3. Experiment 2: Test of the linear dependence of the measured $\Delta B_{z,c}$ on the applied current strength in three subjects, performed for both MESE and SSFP-FID (T_R=120 ms, N_{meas} = 12) with multi-gradient-echo readouts. (a) Magnitude and $\Delta B_{z,c}$ images for the measurements at I_c = 1 mA. The black rectangles depict the regions-of-interest (ROIs), in which the average $\Delta B_{z,c}$ was extracted. In subject S_1, a line-like artifact is visible in the MESE $\Delta B_{z,c}$ images in the phase encoding direction

and to a lesser extent also in the SSFP-FID results. The artifact is consistent with flow effects from vessels. We did not observe this type of artifact again. (b) Dependency of the average $\Delta B_{z,c}$ in the ROI on the applied current strength. For MESE, the results of the two measurements are shown as blue and orange lines, and their average is shown as a green line. For SSFP-FID, the average of the 12 measurements is shown; the bars represent the standard error.

Figure 4. Experiment 3: Correction of the cable-induced magnetic stray fields for SSFP-FID measurements (T_R=120 ms, N_{meas}= 24) with multi-gradient-echo readouts in four subjects (no tissue current). The experiments were repeated twice, and the figure shows the results of the first experimental run. (a) Magnitude images. (b) Uncorrected $\Delta B_{z,c}$ images showing the stray field generated by the current flow in the wire loop around the head. (c) Corrected $\Delta B_{z,c}$ images, in which the stray field was calculated based on the reconstructed wire path and subtracted from the measured $\Delta B_{z,c}$. (d) $\Delta B_{z,c}$ images of the control measurements performed without current injection.

Figure 5. Experiment 4: Comparison of SSFP-FID measurements with multi-gradient-echo readouts performed in five subjects using three different repetition times T_R. (a) $\Delta B_{z,c}$ images of the experiments performed without current injection. (b) $\Delta B_{z,c}$ images of the experiments with current injection. The experiments using T_R = 40 ms exhibit the highest noise levels. The total acquisition time was kept the same for the three repetition times by adapting the number of measurements (T_R=40 ms: N_{meas}= 72; T_R=80 ms: N_{meas}= 36; T_R=120 ms: N_{meas}= 24).

Figure 6. Experiment 5: SSFP-FID measurements (T_R=120 ms, N_{meas}= 24) with multi-gradient-echo readouts of five subjects for the R-L and A-P electrode montages. (a) Magnitude images. (b) Uncorrected $\Delta B_{z,c}$ images (left column: R-L montage; right column: A-P montage). (c) Corrected $\Delta B_{z,c}$ images. The electrode positions are indicated as black boxes. Note that cable contributions dominate the uncorrected images.

Figure 7. Experiment 5: (a) SSFP-FID measurements and FEM simulations of the current-induced $\Delta B_{z,c}$ for subject S1 in Fig. 6. Shown are the MR magnitude image, and the corrected $\Delta B_{z,c}$ images and FEM results for the both the R-L and A-P montages. The electrode positions are shown as black rectangles. (b) Scatter plots of the $\Delta B_{z,c}$ measurements versus simulations (left column: R-L montage; right column: A-P montage). The results are plotted for the cases with (blue) and without (orange) cable-induced $\Delta B_{z,c}$ correction. The results without stray field correction have no correspondence to the simulations. The red regression lines are based on a linear regression of the corrected $\Delta B_{z,c}$ measurement results versus the simulations (please refer to Table 5 for the results of the regression analyses for all five subjects).

Figure 8. Experiment 5: (a) Reconstruction of the current density distributions from simulated and measured $\Delta B_{z,c}$ images. The results for subject S_1 are exemplarily shown (upper row: R-L montage; second row: A-P montage). The norm of the 2D current densities is depicted. Visual comparison of the simulated current density distributions $\vec{J}_{FEM}$ with their corresponding $\vec{J}_{rec}$ images that were reconstructed from the simulated $\Delta B_{z,c}$ images shows that the reconstruction algorithm recovers only the coarse features of the current flow pattern. Specifically, higher current densities close to the electrodes and in the longitudinal fissure are maintained. Visual comparison of the reconstructions from uncorrected and corrected $\Delta B_{z,c}$ measurements reveals that the reconstructions from the uncorrected measurements overestimate the current densities close to the electrodes. For the A-P montage, an increased current flow in the longitudinal fissure is only visible for the corrected measurements. (b) Scatter plots of the projected current flow measurements versus simulations for subject S_1 (1^{st} row: R-L montage; 2^{nd} row: A-P montage). The results are plotted for the cases with (blue) and without (red) cable-induced stray magnetic field correction. The results without stray field correction overestimate the current flow density, resulting in a smaller slope of the fitted regression line (please refer to Table 6 for the results of the regression analyses for all five subjects).

TABLES

	MESE		SSFP-FID	
	N_{GE}=1 $\mu_{\Delta Bz,c}$ ($\sigma_{\Delta Bz,c}$)	N_{GE}=5	N_{GE}=1	N_{GE}=7
S_1	0.066 (0.166)	0.037 (0.086)	-0.043 (0.149)	0.026 (0.123)
S_2	0.126 (0.186)	0.089 (0.117)	-0.024 (0.201)	-0.012 (0.111)
S_3	0.144 (0.150)	-0.035 (0.103)	-0.078 (0.150)	-0.041 (0.151)
Avg	**0.112 (0.167)**	**0.030 (0.102)**	**-0.048 (0.167)**	**-0.009 (0.128)**

Table 1. Experiment 1: Comparison of single- vs. multi-gradient-echo acquisition for the case without current injection in three subjects. The table lists the mean shifts $\mu_{\Delta Bz,c}$ and standard deviations $\sigma_{\Delta Bz,c}$ (given in brackets) of the noise distributions of $\Delta B_{z,c}$ values in the brain. The last row lists the average $\mu_{\Delta Bz,c}$ and average $\sigma_{\Delta Bz,c}$ values across subjects. The units are in nT. For both MESE and SSFP-FID, the multi-gradient-echo acquisitions have lower mean shifts and standard deviations.

	MESE			SSFP-FID		
	$F_{1,6}$ (p)	β_0 in [nT]	β_1 in [nT/mA]	$F_{1,46}$ (p)	β_0 in [nT]	β_1 in [nT/mA]
S_1	57 ($<0.3\cdot10^{-3}$)	-0.05 (0.08)	0.90 (0.12)	46 ($<10^{-6}$)	-0.07 (0.07)	0.80 (0.12)
S_2	50 ($<0.4\cdot10^{-3}$)	0.07 (0.09)	1.03 (0.15)	27 ($<10^{-5}$)	0.02 (0.13)	1.09 (0.21)
S_3	1527 ($<10^{-6}$)	-0.04 (0.02)	1.44 (0.04)	225 ($<10^{-6}$)	-0.01 (0.06)	1.42 (0.10)

Table 2. Experiment 2: Linear fits of the measured dependence of $\Delta B_{z,c}$ on the applied current strength. The table lists the F- and p-values, the intercepts β_0 and the slopes β_1 of the fitted linear regression models. The standard errors of β_0 and β_1 are given in brackets.

	1st Experiment		**2nd Experiment**	
	I_c=0 mA $\mu_{\Delta Bz,c}$ ($\sigma_{\Delta Bz,c}$)	**I_c=1 mA, corrected**	**I_c=0 mA**	**I_c=1 mA, corrected**
S_1	0.013 (0.136)	0.049 (0.138)	0.016 (0.095)	-0.011 (0.194)
S_2	-0.067 (0.120)	-0.012 (0.148)	-0.022 (0.091)	0.012 (0.133)
S_3	-0.110 (0.110)	-0.169 (0.130)	0.011 (0.108)	-0.018 (0.129)
S_4	0.031 (0.072)	0.110 (0.170)	0.103 (0.096)	-0.080 (0.125)
Avg	**-0.033 (0.110)**	**-0.006 (0.147)**	**0.027 (0.098)**	**-0.024 (0.145)**

Table 3. Experiment 3: Correction of the cable-induced magnetic stray field for SSFP-FID measurements in four subjects. The experiment was repeated twice. The table lists the mean shifts $\mu_{\Delta Bz,c}$ and standard deviations $\sigma_{\Delta Bz,c}$ (given in brackets) of the distribution of $\Delta B_{z,c}$ in the brain. The last row lists the average $\mu_{\Delta Bz,c}$ and average $\sigma_{\Delta Bz,c}$ values across subjects. The units are in nT. Correcting the stray field induced by the wire loop around the head results in noise distributions, which are similar to those of the control measurements without current injection.

	T_R = 40 ms $\mu_{\Delta Bz,c}$ ($\sigma_{\Delta Bz,c}$)	**T_R = 80 ms**	**T_R = 120 ms**
S_1	0.039 (0.202)	0.115 (0.092)	-0.046 (0.111)
S_2	-0.012 (0.191)	-0.007 (0.073)	-0.026 (0.095)
S_3	-0.045 (0.212)	0.053 (0.076)	0.011 (0.090)
S_4	-0.042 (0.259)	0.049 (0.084)	0.179 (0.210)
S_5	-0.002 (0.192)	-0.052 (0.091)	0.038 (0.084)
Avg	**-0.012 (0.211)**	**0.031 (0.083)**	**0.031 (0.100)**

Table 4. Experiment 4: Comparison of SSFP-FID measurements performed in five subjects without current injection for three different repetition times T_R. The table lists the mean shifts $\mu_{\Delta Bz,c}$ and standard deviations $\sigma_{\Delta Bz,c}$ (given in brackets) of the noise distributions of $\Delta B_{z,c}$ in the brain. The last row lists the average $\mu_{\Delta Bz,c}$ and average $\sigma_{\Delta Bz,c}$ values across subjects. The units are in nT. Both the

measurements at T_R = 80 ms and 120 ms exhibit lower noise standard deviations than the measurements at T_R = 40 ms.

	R-L			A-P		
	β_0 in [nT]	β_1	R^2	β_0 in [nT]	β_1	R^2
S_1	0.18 ±0.002	0.81 ±0.12	0.87	0.04 ±0.003	0.80 ±0.004	0.91
S_2	0.04 ±0.003	0.75 ±0.15	0.80	0.06 ±0.004	0.87 ±0.005	0.90
S_3	-0.06 ±0.003	0.71 ±0.04	0.59	0.08 ±0.004	1.04 ±0.008	0.84
S_4	0.30 ±0.005	0.97 ±0.01	0.69	-0.14 ±0.003	0.84 ±0.005	0.89
S_5	0.10 ±0.006	0.77 ±0.02	0.44	-0.01 ±0.003	0.94 ±0.006	0.87
Avg ±SE	**0.11 ±0.06**	**0.80 ±0.05**	**0.68 ±0.08**	**0.01 ±0.04**	**0.90 ±0.04**	**0.88 ±0.01**

Table 5. Experiment 5: Linear fits of the $\Delta B_{z,c}$ measurements and simulations across five different subjects for the two current injection profiles (R-L and A-P). The table lists the intercepts β_0, the slopes β_1, and the coefficient of determination R^2 of the fitted linear regression models. For β_0 and β_1, also the standard errors are stated. The last row lists the averages across subjects, and the standard error of the averages. Most estimated slopes are lower than unity (i.e., the simulations slightly underestimate the $\Delta B_{z,c}$). The significance of the regression models was confirmed using F-tests, with the results being highly significant ($p<10^{-6}$) in all cases.

	R-L					
	Uncorrected			Corrected		
	β_0 in [A/m^2]	β_1	R^2	β_0 in [A/m^2]	β_1	R^2
S_1	0.021 $\pm$0.001	0.56 $\pm 6.4 \cdot 10^{-3}$	0.68	0.018 $\pm$0.001	0.68 $\pm 8.7 \cdot 10^{-3}$	0.63
S_2	0.016 $\pm$0.001	0.71 $\pm 6.6 \cdot 10^{-3}$	0.75	0.014 $\pm$0.001	0.78 $\pm 7.5 \cdot 10^{-3}$	0.74
S_3	0.016 $\pm$0.001	0.69 $\pm 7.4 \cdot 10^{-3}$	0.73	0.007 $\pm$0.001	0.89 $\pm 8.9 \cdot 10^{-3}$	0.76
S_4	0.018 $\pm$0.001	0.61 $\pm 10.7 \cdot 10^{-3}$	0.53	0.014 $\pm$0.001	0.74 $\pm 9.2 \cdot 10^{-3}$	0.69
S_5	0.019 $\pm$0.001	0.65 $\pm 6.8 \cdot 10^{-3}$	0.74	0.011 $\pm$0.001	0.80 $\pm 7.4 \cdot 10^{-3}$	0.79
Avg $\pm$SE	**0.018 $\pm$0.001**	**0.64 $\pm$0.03**	**0.69 $\pm$0.04**	**0.013 $\pm$0.002**	**0.78 $\pm$0.03**	**0.72 $\pm$0.03**

Table 6. Experiment 5: Linear fits of the current density distributions reconstructed from measurements and simulations. Listed are the results for the current injection profile R-L, for both the cases with and without stray magnetic field correction. The table lists the intercepts β_0, the slopes β_1, and the coefficient of determination R^2 of the fitted linear regression models. For β_0 and β_1, also the standard errors are stated. The last row lists the averages across subjects, and the standard error of the averages. The estimated slopes increase on average by 0.14 for the corrected vs. uncorrected case. Also for the corrected case, the estimated slopes are still lower than unity (i.e., the simulations underestimate the current density). The significance of the regression models was confirmed using F-tests, with the results being highly significant ($p<10^{-6}$) in all cases.

	A-P					
	Uncorrected			Corrected		
	β_0 in [A/m^2]	β_1	R^2	β_0 in [A/m^2]	β_1	R^2
S_1	0.032 $\pm$0.001	0.49 $\pm 7.4\cdot10^{-3}$	0.55	0.023 $\pm$0.001	0.71 $\pm 9.2\cdot10^{-3}$	0.62
S_2	0.022 $\pm$0.001	0.67 $\pm 6.4\cdot10^{-3}$	0.74	0.015 $\pm$0.001	0.84 $\pm 7.9\cdot10^{-3}$	0.75
S_3	0.022 $\pm$0.001	0.70 $\pm 9.0\cdot10^{-3}$	0.65	0.014 $\pm$0.001	0.83 $\pm 10.8\cdot10^{-3}$	0.65
S_4	0.023 $\pm$0.001	0.79 $\pm 10.2\cdot10^{-3}$	0.68	0.009 $\pm$0.001	0.84 $\pm 10.2\cdot10^{-3}$	0.71
S_5	0.018 $\pm$0.001	0.67 $\pm 6.5\cdot10^{-3}$	0.77	0.010 $\pm$0.001	0.91 $\pm 7.6\cdot10^{-3}$	0.82
Avg $\pm$SE	**0.023 $\pm$0.002**	**0.66 $\pm$0.05**	**0.68 $\pm$0.04**	**0.014 $\pm$0.003**	**0.83 $\pm$0.03**	**0.71 $\pm$0.04**

Table 7. Experiment 5: Linear fits of the current density distributions reconstructed from measurements and simulations. Listed are the results for the current injection profile A-P. The estimated slopes increase on average by 0.16 for the corrected vs. uncorrected case. The estimated slopes are still lower than unity also for the corrected case (i.e., the simulations underestimates the current density). This is similar to the results observed for current injection profile R-L. The significance of the regression models was confirmed using F-tests, with the results being highly significant ($p<10^{-6}$) in all cases.

References

Bieri, O., Maderwald, S., Ladd, M.E., Scheffler, K., 2006. Balanced alternating steady-state elastography. Magn. Reson. Med. 55, 233–41.

Birgül, Ö., Eyüboğlu, B.M., Ider, Y.Z., 2003. Experimental results for 2D magnetic resonance electrical impedance tomography (MR-EIT) using magnetic flux density in one direction. Phys. Med. Biol. 48, 3485–3504.

Dabek, J., Kalogianni, K., Rotgans, E., van der Helm, F.C.T., Kwakkel, G., van Wegen, E.E.H., Daffertshofer, A., de Munck, J.C., 2016. Determination of head conductivity frequency response in vivo with optimized EIT-EEG. Neuroimage 127, 484–495. doi:10.1016/j.neuroimage.2015.11.023

Eyüboğlu, B.M., 2006a. Electrical Impedance Imaging, Injected Current, in: Wiley Encyclopedia of Biomedical Engineering. pp. 1195–1205.

Eyüboğlu, B.M., 2006b. Magnetic Resonance Current Density Imaging, in: Wiley Encyclopedia of Biomedical Engineering. pp. 2147–53.

Eyüboğlu, B.M., 2006c. Magnetic Resonance-Electrical Impedance Tomography, in: Wiley Encyclopedia of Biomedical Engineering. pp. 2154–62.

Faes, T.J.C., Meij, H.A. van der, Munck, J.C. de, Heethaar, R.M., 1999. The electric resistivity of human tissues (100 Hz-10 MHz): a meta-analysis of review studies. Physiol. Meas. 20, R1–R10. doi:10.1088/0967-3334/20/4/201

Göksu, C., Sadighi, M., Eroğlu, H.H., Eyüboğlu, M., 2014. Realization of Magnetic Resonance Current Density Imaging at 3 Tesla, in: Annual International Conference of the IEEE Engineering in Medicine and Biology Society - EMBC. pp. 1115–1118.

Göksu, C., Scheffler, K., Ehses, P., Hanson, L.G., Thielscher, A., 2017. Sensitivity Analysis of Magnetic Field Measurements for Magnetic Resonance Electrical Impedance Tomography (MREIT). Magn. Reson. Med. 0. doi:10.1002/mrm.26727

Haase, A., Frahm, J., Hänicke, W., Matthaei, D., 1985. 1H NMR chemical shift selective (CHESS) imaging. Phys. Med. Biol. 30, 341–344.

Han, Y.Q., Meng, Z.J., Jeong, W.C., Kim, Y.T., Minhas, A.S., Kim, H.J., Nam, H.S., Kwon, O., Woo, E.J., 2010. MREIT conductivity imaging of canine head using multi-echo pulse sequence. J. Phys. Conf. Ser. 224, 12078. doi:10.1088/1742-6596/224/1/012078

Huang, Y., Liu, A.A., Lafon, B., Friedman, D., Dayan, M., Wang, X., Bikson, M., Doyle, W.K., Devinsky, O., Parra, L.C., 2017. Measurements and models of electric fields in the in vivo human brain during transcranial electric stimulation. Elife 6, e18834. doi:10.7554/eLife.18834

Ida, M., Wakayama, T., Nielsen, M.L., Abe, T., Grodzki, D.M., 2015. Quiet T1-Weighted Imaging Using PETRA : Initial Clinical Evaluation in Intracranial Tumor Patients. J. Magn. Reson. Imaging 41, 447–453. doi:10.1002/jmri.24575

Ider, Y.Z., Birgül, Ö., 1998. Use of the magnetic field generated by the internal distribution of injected currents for Electrical Impedance Tomography (MR-EIT). ELEKTRİK 6, 215–225.

Ider, Y.Z., Birgül, Ö., Oran, Ö.F., Arıkan, O., Hamamura, M.J., Müftüler, T., 2010. Fourier transform magnetic resonance current density imaging (FT-MRCDI) from one component of magnetic flux density. Phys. Med. Biol. 55, 3177–3199. doi:10.1088/0031-9155/55/11/013

Jaynes, E.T., 1955. Matrix treatment of nuclear induction. Phys. Rev. 98, 1099–1105.

Jeon, K., Minhas, A.S., Kim, Y.T., Jeong, W.C., Kim, H.J., Kang, B.T., Park, H.M., Lee, C.-O., Seo, J.K., Woo, E.J., 2009. MREIT conductivity imaging of the postmortem canine abdomen using CoReHA. Physiol. Meas. 30, 957–66. doi:10.1088/0967-3334/30/9/007

Jeong, W.C., Kim, Y.T., Minhas, a S., Lee, T.H., Kim, H.J., Nam, H.S., Kwon, O., Woo, E.J., 2010. In vivo conductivity imaging of human knee using 3 mA injection current in MREIT. J. Phys. Conf. Ser. 224, 12148. doi:10.1088/1742-6596/224/1/012148

Jog, M. V, Smith, R.X., Jann, K., Dunn, W., Lafon, B., Truong, D., Wu, A., Parra, L., Bikson, M., Wang, D.J.J., 2016. In-vivo Imaging of Magnetic Fields Induced by Transcranial Direct Current Stimulation (tDCS) in Human Brain using MRI. Sci. Rep. 6, 34385. doi:10.1038/srep34385

Joy, M.L.G., 2004. MR current density and conductivity imaging: the state of the art., in: Conf Proc IEEE Eng Med Biol Soc. pp. 5315–9. doi:10.1109/IEMBS.2004.1404484

Kasinadhuni, A.K., Indahlastari, A., Chauhan, M., Scär, M., Mareci, T.H., Sadleir, R.J., 2017. Imaging of current flow in the human head during transcranial electrical therapy. Brain Stimul. 10, 764–772. doi:10.1016/j.brs.2017.04.125

Kim, H.J., Kim, Y.T., Minhas, A.S., Jeong, W.C., Woo, E.J., 2009. In Vivo High-Resolution Conductivity Imaging of the Human Leg Using MREIT : The First Human Experiment 28, 1681–1687.

Kim, H.J., Oh, T.I., Kim, Y.T., Lee, B. Il, Woo, E.J., Seo, J.K., Lee, S.Y., Kwon, O., Park, C., Kang, B.T., Park, H.M., 2008. In vivo electrical conductivity imaging of a canine brain using a 3 T MREIT system. Physiol. Meas. 29, 1145–55. doi:10.1088/0967-3334/29/10/001

Kim, Y.T., Minhas, A.S., Meng, Z., Kim, H.J., Woo, E.J., 2011. Conductivity imaging of human lower extremity using MREIT with multi-echo pulse sequence and 3 mA imaging current. 2011 8th Int. Symp. Noninvasive Funct. Source Imaging Brain Hear. 2011 8th Int. Conf. Bioelectromagn. 48–52. doi:10.1109/NFSI.2011.5936818

Kwon, O.I., Sajib, S.Z., Sersa, I., Oh, T.I., Jeong, W.C., Kim, H.J., Woo, E.J., 2016. Current Density Imaging During Transcranial Direct Current Stimulation Using DT-MRI and MREIT: Algorithm Development and Numerical Simulations. IEEE Trans Biomed Eng 63, 168–175. doi:10.1109/TBME.2015.2448555

Lee, C., Jeon, K., Ahn, S., Kim, H.J., Woo, E.J., Member, S., 2011. Ramp-Preserving Denoising for Conductivity Image Reconstruction in Magnetic Resonance Electrical Impedance Tomography 58, 2038–2050.

Lee, H., Jeong, W.C., Kim, H.J., Woo, E.J., Park, J., 2016. Alternating steady state free precession for estimation of current-induced magnetic flux density: A feasibility study. Magn. Reson. Med. 75, 2009–2019.

Meng, Z., Sajib, S.Z., Chauhan, M., Jeong, W.C., Kim, Y.T., Kim, H.J., Woo, E.J., 2012. Improved conductivity image of human lower extremity using MREIT with chemical shift artifact correction. Biomed. Eng. Lett. 2, 62–68. doi:10.1007/s13534-012-0052-0

Minhas, A.S., Woo, E.J., Sadleir, R., 2010. Simulation of MREIT using balanced steady state free precession (b-SSFP) pulse sequence. J. Phys. Conf. Ser. 224, 12019. doi:10.1088/1742-6596/224/1/012019

Miranda, P.C., 2013. Physics of effects of transcranial brain stimulation. Handb. Clin. Neurol. 116, 353–366.

Mosher, J.C., Leahy, R.M., Lewis, P.S., 1999. EEG and MEG: Forward Solutions for Inverse Methods. IEEE Trans. Biomed. Eng. 46, 245–259.

Nam, H.S., Kwon, O.I., 2010. Optimization of multiply acquired magnetic flux density B(z) using ICNE-Multiecho train in MREIT. Phys. Med. Biol. 55, 2743–59.

Nicholson, P.W., 1965. Specific impedance of cerebral white matter. Exp. Neurol. 13, 386–401. doi:10.1016/0014-4886(65)90126-3

Nitsche, M.A., Paulus, W., 2000. Excitability changes induced in the human motor cortex by weak transcranial direct current stimulation. J. Physiol. 527, 633–639.

Oh, S.H., Lee, B. Il, Woo, E.J., Lee, S.Y., Cho, M.H., Kwon, O., Seo, J.K., 2003. Conductivity and current density image reconstruction using harmonic Bz algorithm in magnetic resonance electrical impedance tomography. Phys. Med. Biol. 48, 3101–3116. doi:10.1088/0031-9155/48/19/001

Oh, S.H., Lee, B. Il, Woo, E.J., Lee, S.Y., Kim, T.-S., Kwon, O., Seo, J.K., 2005. Electrical conductivity images of biological tissue phantoms in MREIT. Physiol. Meas. 26, S279-88. doi:10.1088/0967-3334/26/2/026

Oostenveld, R., Fries, P., Maris, E., Schoffelen, J.M., 2011. FieldTrip: Open source software for advanced analysis of MEG, EEG, and invasive electrophysiological data. Comput. Intell. Neurosci. 2011. doi:10.1155/2011/156869

Opitz, A., Falchier, A., Yan, C.-G., Yeagle, E.M., Linn, G.S., Megevand, P., Thielscher, A., Deborah A., R., Milham, M.P., Mehta, A.D., Schroeder, C.E., 2016. Spatiotemporal structure of intracranial electric fields induced by transcranial electric stimulation in humans and nonhuman primates. Sci. Rep. 6, 31236. doi:10.1038/srep31236

Opitz, A., Windhoff, M., Heidemann, R.M., Turner, R., Thielscher, A., 2011. How the brain tissue shapes the electric field induced by transcranial magnetic stimulation. Neuroimage 58, 849–859. doi:10.1016/j.neuroimage.2011.06.069

Park, C., Lee, B. Il, Kwon, O.I., 2007. Analysis of recoverable current from one component of magnetic flux density in MREIT and MRCDI. Phys. Med. Biol. 52, 3001–13. doi:10.1088/0031-9155/52/11/005

Sadighi, M., Göksu, C., Eyüboğlu, B.M., 2014. J-based Magnetic Resonance Conductivity Tensor Imaging (MRCTI) at 3 T. Annu. Int. Conf. IEEE Eng. Med. Biol. Soc. - EMBC 1139–1142.

Sadleir, R.J., Grant, S.C., Silver, X., Zhang, S.U., Woo, E.J., Lee, S.Y., Kim, T.S., Oh, S.H., Lee, B.I., Seo, J.K., 2005. Magnetic Resonance Electrical Impedance Tomography (MREIT) at 11 Tesla Field Strength : Preliminary Experimental Study 7, 340–343.

Sajib, S.Z.K., Kim, H.J., Kwon, O.I., Woo, E.J., 2012. Regional absolute conductivity reconstruction using projected current density in MREIT. Phys. Med. Biol. 57, 5841–5859. doi:10.1088/0031-9155/57/18/5841

Saturnino, G.B., Antunes, A., Thielscher, A., 2015. On the importance of electrode parameters for shaping electric field patterns generated by tDCS. Neuroimage 120, 25–35. doi:10.1016/j.neuroimage.2015.06.067

Scheffler, K., Maderwald, S., Ladd, M.E., Bieri, O., 2006. Oscillating steady states. Magn. Reson. Med. 55, 598–603.

Scott, G.C., Joy, M.L.G., Armstrong, R.L., Henkelman, R.M., 1992. Sensitivity of magnetic-resonance current-density imaging. J. Magn. Reson. 97, 235–254.

Scott, G.C., Joy, M.L.G., Armstrong, R.L., Henkelman, R.M., 1991. Measurement of nonuniform current density by magnetic resonance. IEEE Trans. Med. Imaging 10, 362–374.

Seo, J.K., Woo, E.J., 2011. Magnetic Resonance Electrical Impedance Tomography. Soc. Ind. Appl. Math. 53, 40–68.

Seo, J.K., Yoon, J., Woo, E.J., Kwon, O., 2003. Reconstruction of Conductivity and Current Density Images Using Only One Component of Magnetic Field Measurements. IEEE Trans. Biomed. Eng. 50, 1121–1124.

Tadel, F., Baillet, S., Mosher, J.C., Pantazis, D., Leahy, R.M., 2011. Brainstorm: A User-Friendly Application for MEG/EEG Analysis. Comput. Intell. Neurosci. 2011, 1–13. doi:10.1155/2011/879716

Thielscher, A., Antunes, A., Saturnino, G.B., 2015. Field modeling for transcranial magnetic stimulation: A useful tool to understand the physiological effects of TMS?, in: Proceedings of the Annual International Conference of the IEEE Engineering in Medicine and Biology Society, EMBS. pp. 222–225. doi:10.1109/EMBC.2015.7318340

Thielscher, A., Opitz, A., Windhoff, M., 2011. Impact of the gyral geometry on the electric field induced by transcranial magnetic stimulation. Neuroimage 54, 234–243.

Utz, K.S., Dimova, V., Oppenländer, K., Kerkhoff, G., 2010. Electrified minds: Transcranial direct current stimulation (tDCS) and Galvanic Vestibular Stimulation (GVS) as methods of non-invasive brain stimulation in neuropsychology-A review of current data and future implications. Neuropsychologia 48, 2789–2810.

Walsh, D.O., Gmitro, A.F., Marcellin, M.W., 2000. Adaptive reconstruction of phased array MR imagery. Magn. Reson. Med. 43, 682–690.

Woo, E.J., Lee, S.Y., Mun, C.W., 1994. Impedance Tomography Using Internal Current Density Distribution Measured by Nuclear Magnetic Resonance. SPIE 2299, 377–385.

Woo, E.J., Seo, J.K., 2008. Magnetic resonance electrical impedance tomography (MREIT) for high-resolution conductivity imaging. Physiol. Meas. 29, R1-26. doi:10.1088/0967-3334/29/10/R01

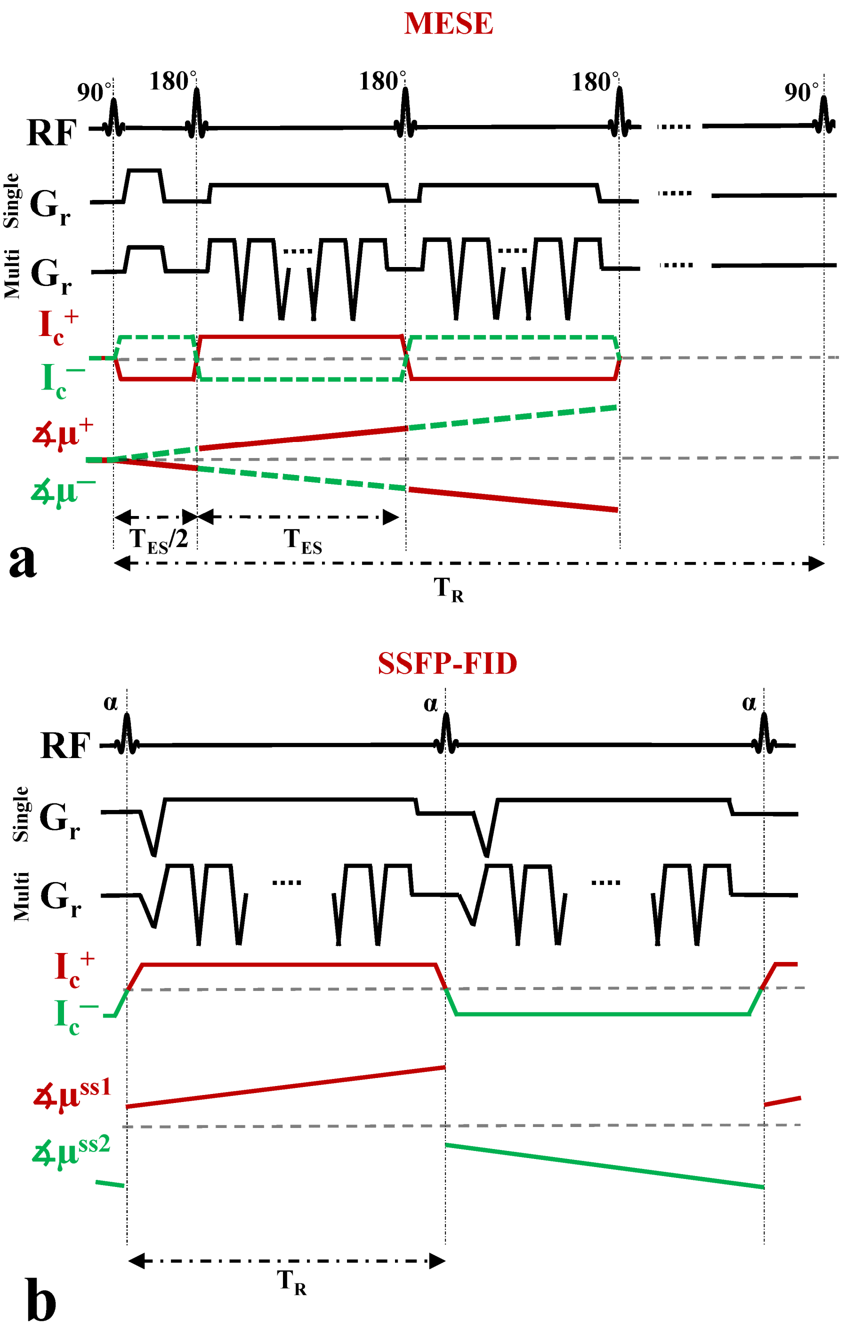
MESE
90°
180°
180°
180°
90°
RF
Single
G_r
Multi
G_r
I_c^+
I_c^-
$\measuredangle\mu^+$
$\measuredangle\mu^-$
$T_{ES}/2$
T_{ES}
a
T_R
SSFP-FID
α
α
α
RF
Single
G_r
Multi
G_r
I_c^+
I_c^-
$\measuredangle\mu^{ss1}$
$\measuredangle\mu^{ss2}$
T_R
b

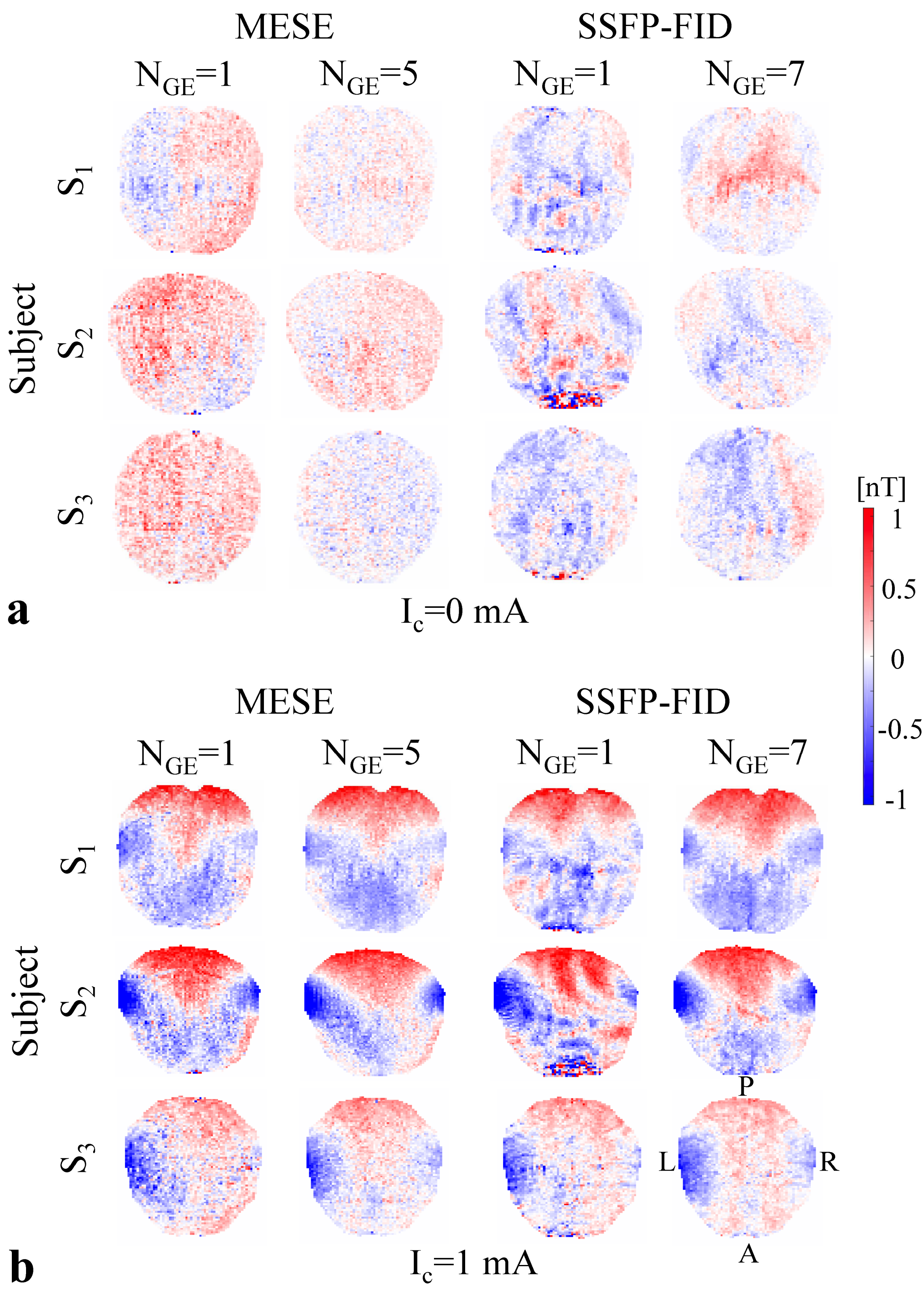
MESE
SSFP-FID
N_{GE}=1
N_{GE}=5
N_{GE}=1
N_{GE}=7
Subject
S_1
S_2
S_3
a
I_c=0 mA
[nT]
1
0.5
0
-0.5
-1
MESE
SSFP-FID
N_{GE}=1
N_{GE}=5
N_{GE}=1
N_{GE}=7
Subject
S_1
S_2
S_3
P
L
R
A
b
I_c=1 mA

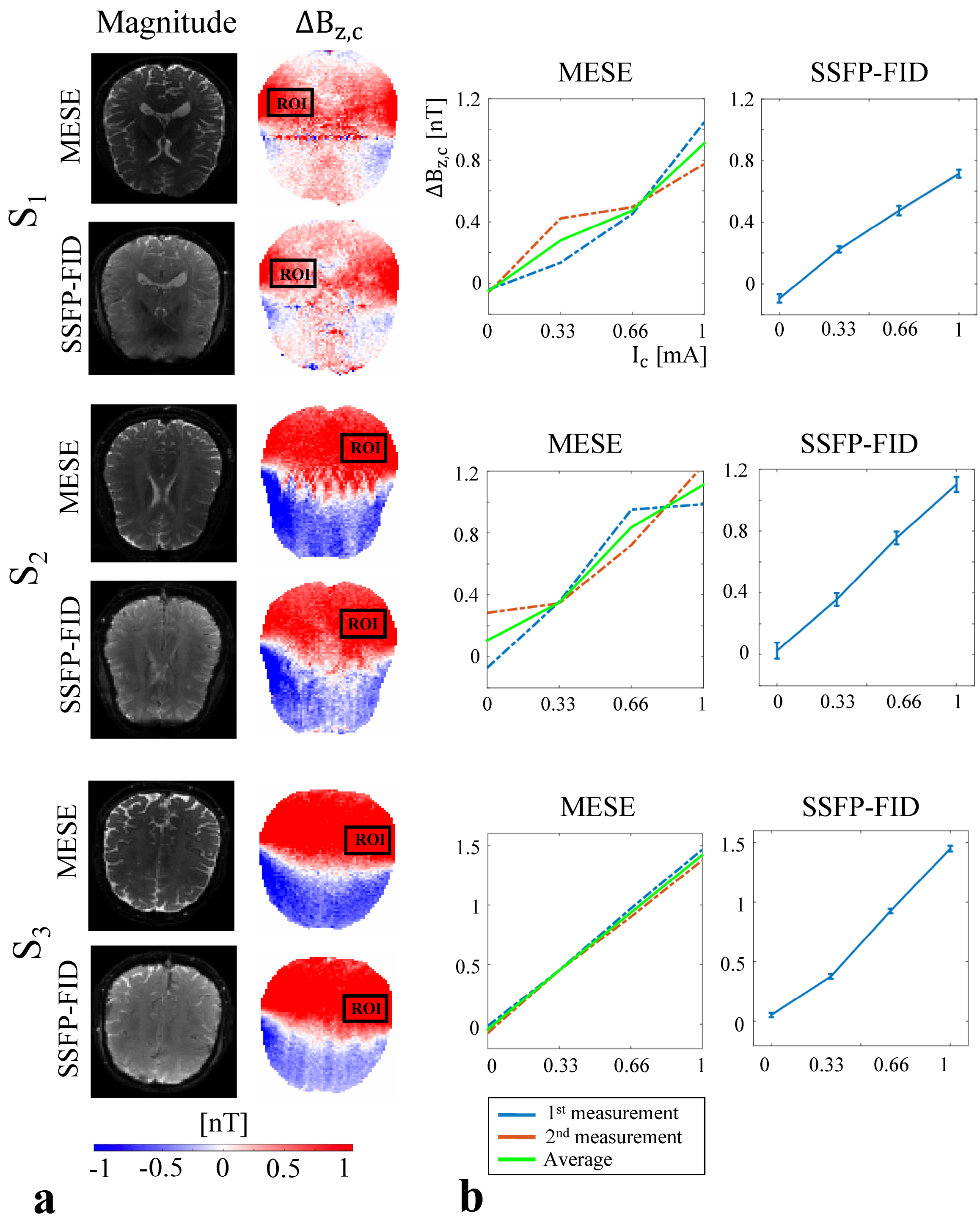

Magnitude
ΔBz,c
S1
S2
S3
MESE
SSFP-FID
ROI
[nT]
-1 -0.5 0 0.5 1
a
MESE
SSFP-FID
ΔBz,c [nT]
Ic [mA]
0 0.33 0.66 1
1st measurement
2nd measurement
Average
b

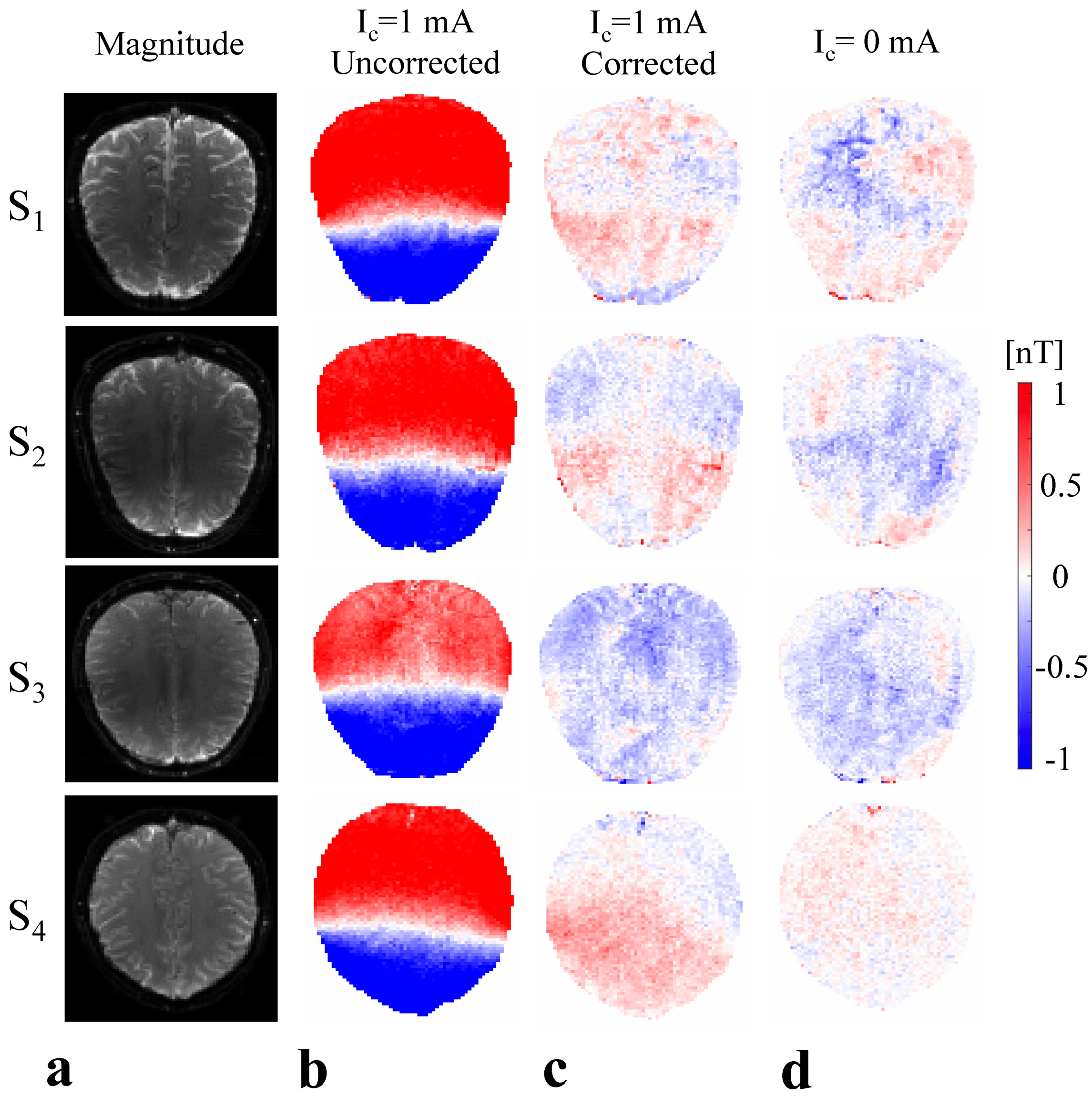
Magnitude
I_c=1 mA Uncorrected
I_c=1 mA Corrected
I_c= 0 mA
S_1
S_2
S_3
S_4
[nT]
1
0.5
0
-0.5
-1
a
b
c
d

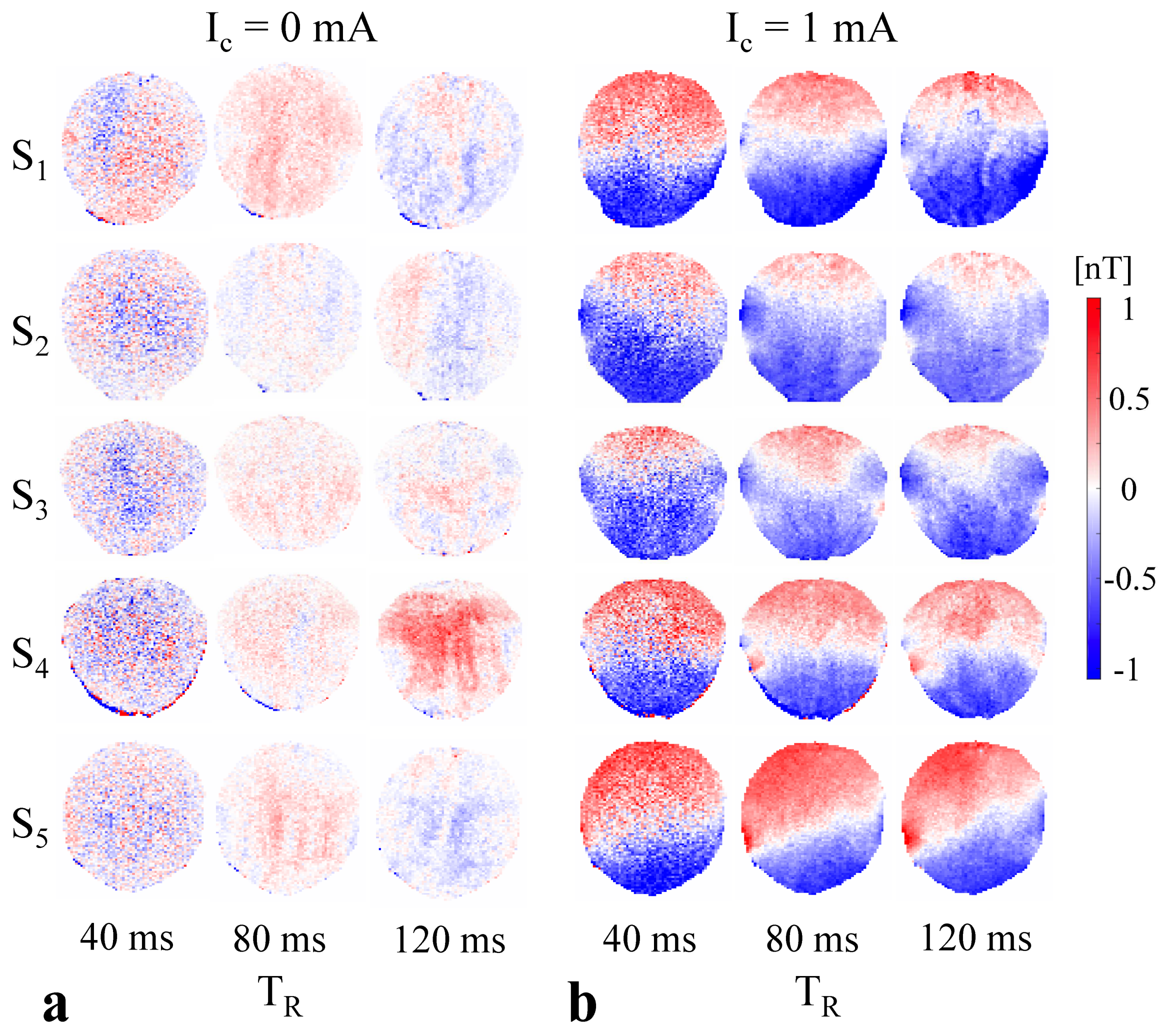

I_c = 0 mA
I_c = 1 mA
S_1
S_2
S_3
S_4
S_5
[nT]
1
0.5
0
-0.5
-1
40 ms
80 ms
120 ms
40 ms
80 ms
120 ms
a
T_R
b
T_R

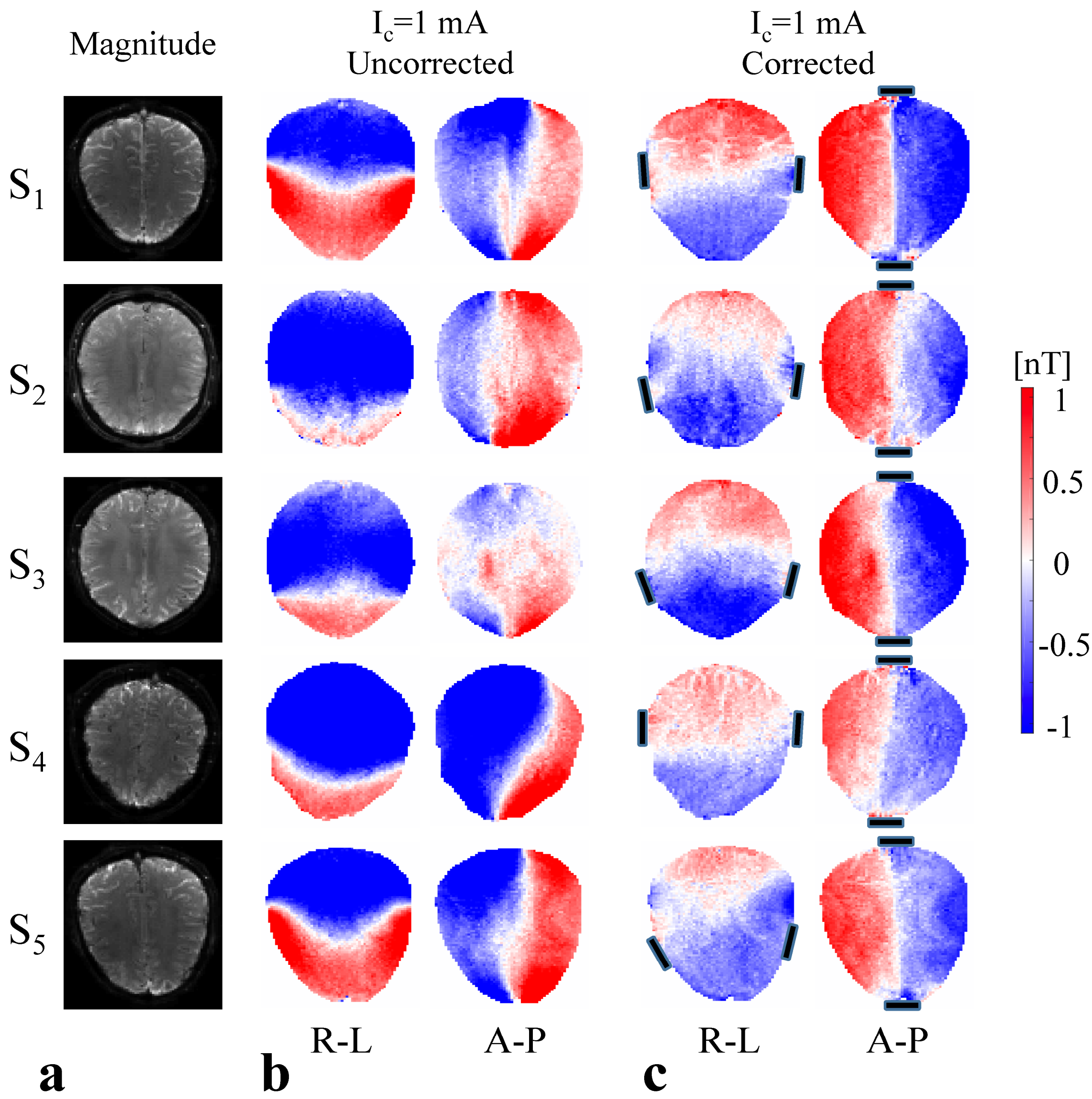

Magnitude
I_c=1 mA
Uncorrected
I_c=1 mA
Corrected
S_1
S_2
S_3
S_4
S_5
[nT]
1
0.5
0
-0.5
-1
R-L
A-P
R-L
A-P
a
b
c

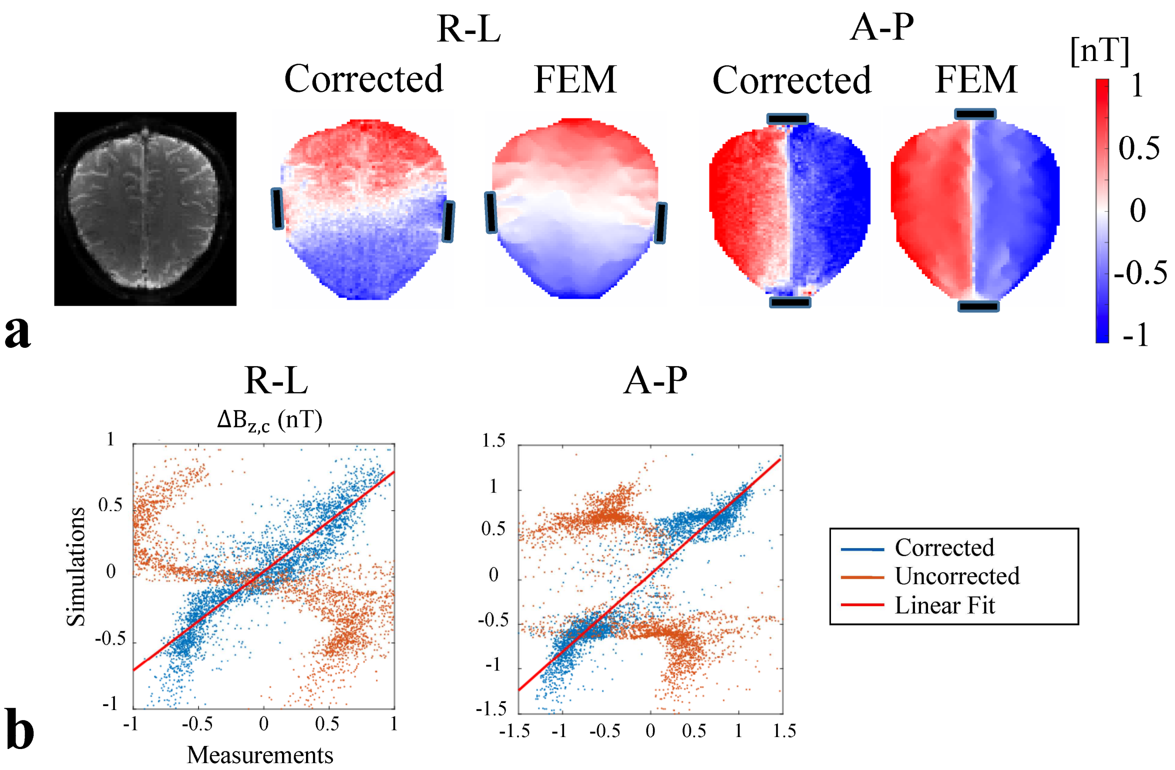
R-L
Corrected
FEM
A-P
Corrected
FEM
[nT]
1
0.5
0
-0.5
-1
a
R-L
ΔB z,c (nT)
Simulations
Measurements
1
0.5
0
-0.5
-1
A-P
1.5
1
0.5
0
-0.5
-1
-1.5
Corrected
Uncorrected
Linear Fit
b

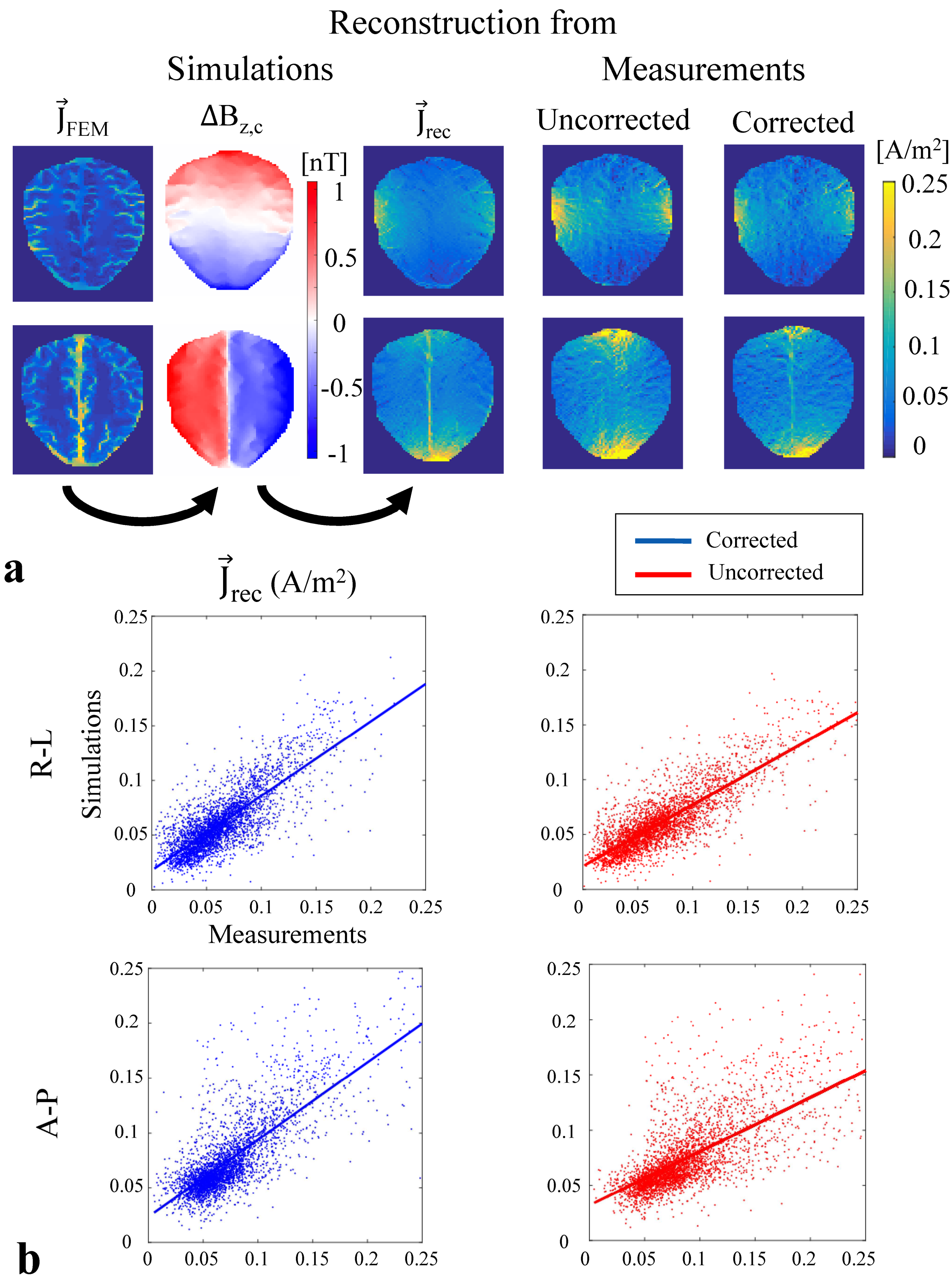
Reconstruction from
Simulations
Measurements
$\vec{J}_{FEM}$
$\Delta B_{z,c}$
$\vec{J}_{rec}$
Uncorrected
Corrected
[nT]
1
0.5
0
-0.5
-1
[A/m²]
0.25
0.2
0.15
0.1
0.05
0
a
Corrected
Uncorrected
$\vec{J}_{rec}$ (A/m²)
R-L
Simulations
Measurements
A-P
b